Materials Today Bio 20 (2023) 100650

Contents lists available at ScienceDirect

Materials Today Bio

journal homepage: www.journals.elsevier.com/materials-today-bio

Colorimetric pH-responsive and hemostatic hydrogel-based bioadhesives containing functionalized silver nanoparticles

Elham Khadem [a], Mahshid Kharaziha [a,b,**], Sahar Salehi [b,*]

[a] Department of Materials Engineering, Isfahan University of Technology, 84156-83111, Isfahan, Iran
[b] Department of Biomaterials, University of Bayreuth, 95447, Bayreuth, Germany

ARTICLE INFO

Keywords:
Oxidized sodium alginate
Carboxyethyl chitosan
pH-responsive
Bioadhesives
Wound healing

ABSTRACT

Here we develop and characterize a dual-cross-linked pH-responsive hydrogel based on the carboxyethyl chitosan-oxidized sodium alginate (CAO) containing silver nanoparticles (Ag NPs) functionalized with tannic acid/red cabbage (ATR). This hybrid hydrogel is formed via covalent and non-covalent cross-linking. The adhesive strength measured in contact with cow skin and compression strength is measured more than 3 times higher than that of CAO. Importantly, the incorporation of 1 wt% ATR into CAO significantly enhances the compression strength of CAO from 35.1 ± 2.1 kPa to 97.5 ± 2.9 kPa. Moreover, the cyclic compression tests confirm significantly higher elastic behavior of CAO after the addition of ATR-functionalized NPs to CAO. The CAO/ATR hydrogel is pH-sensitive and indicated remarkable color changes in different buffer solutions. The CAO/ATR also shows improved hemostatic properties and reduced clotting time compared to the clotting time of blood in contact with CAO hydrogel. In addition, while CAO/ATR is effective in inhibiting the growth of both Gram-positive and Gram-negative bacteria, CAO is only effective in inhibiting the growth of Gram-positive bacteria. Finally, the CAO/ATR hydrogel is cytocompatible with L929 fibroblasts. In summary, the resulting CAO/ATR hydrogel shows promising results in designing and constructing smart wound bioadhesives with high cytocompatibility, antibacterial properties, blood coagulation ability, and fast self-healing properties.

1. Introduction

Bioadhesives are materials that can adhere to either hard or soft tissues (e.g. bones, muscles, ligaments, tendons). Numerous applications of bioadhesives are as wound dressings, tissue sealants, and biomedical implants applied for wound healing, hemostasis, and sealing of damaged tissues [1–4]. Bioadhesives are most widely used as an alternative to, or in addition to, classical materials used for closing surgical sites. Bioadhesives are highly favored due to their ease of use and rapid application (injectable hydrogels). Furthermore, they can be functionalized or loaded with growth factors to promote healing and attract certain cell types to the wound area.

The ability to establish hemostasis and to immediately adhere to tissues are the main requirements of adhesive materials used for wound treatment applications. Furthermore, adhesive hydrogels should be biocompatible and degrade quickly without any negative effects on the host tissues [5]. The wound is a dynamic environment and is affected by both external and intrinsic variables, therefore, it is critical to introduce an ideal hemostatic bioadhesive with an antibacterial ability to prevent the infection while it can track and record the physiochemical and physiological changes in the wound. Such collected data from the wound can be additional qualitative indicators of how well the wound is healing [6]. Among these properties, the introduction of a naked-eye colorimetric sensor is particularly valuable to evaluate the healing process of the wound in a simple way [7,8]. In the last decades, several research groups have developed pH sensors that are electrochemical or colorimetric in nature and can continually monitor skin state [9,10]. The pH value within a wound milieu is an important parameter for therapeutic interventions in wound care as it both reflects and influences numerous fundamental physiological and biochemical processes evolved in wound remodeling. Under normal circumstances, the skin's surface is acidic, with a pH ranging from 4 to 6, which supports the skin's natural barrier function and helps to counteract microbial colonization. However, this acidic milieu is easily affected by wounds that cause fluidic mixing with the body's internal fluid, whose pH value is 7.4. Clinical investigations have demonstrated that the pH of chronic and infected wounds exists in

* Corresponding author.
** Corresponding author. Department of Materials Engineering, Isfahan University of Technology, 84156-83111, Isfahan, Iran.
E-mail addresses: kharaziha@cc.iut.ac.ir (M. Kharaziha), Sahar.Salehi@uni-bayreuth.de (S. Salehi).

https://doi.org/10.1016/j.mtbio.2023.100650
Received 14 December 2022; Received in revised form 27 April 2023; Accepted 29 April 2023
Available online 1 May 2023

the range of 7.5–8.9, which is an alkaline environment. Within this alkaline condition, the healing progression is decreased when compared to the wounds with a pH close to neutral; however as healing evolves, the pH value of wound changes to a neutral and then to an acidic state. Therefore, pH is an important indicator of wound healing. Considering the importance of the wound pH, monitoring the pH as an implemented feature in tissue bioadhesives can be helpful in wound management and in determining effective clinical treatment strategies. In recent years, sensors are developed that upon making conformal contact with the skin without causing any restriction in skin motion can monitor pH in wounds [11,12]. Colorimetric hydrogel sensors incorporating pH-sensitive materials and luminous dyes for skin pH measurement are among such sensors that are reliable and easy to read, and can be used without a need for integrated electronics [13–15]. However, the uptake of large volumes of water and exudates while preventing the dye from seeping out of the dressing onto the skin is a major issue for the production and usage of luminescence systems [16,17]. For such applications, hydrogel-based tissue adhesives are favorable due to their ease of application, effective sealing, and desired biocompatibility and biodegradability. They have also been excellent candidates for use as a substrate in dye-based systems [1,18]. However, creating flexible, antibacterial, and hemostatic hydrogel-based adhesives that can develop conformal contact with skin is a significant challenge. The incorporation of appropriate fillers into a hydrogel can provide all of these properties at the same time, suggesting great promise in a variety of applications, such as wound dressing [19].

Derivatives of chitosan and alginate, which have been derived from natural polysaccharides, are broadly applied as bioadhesive hydrogels for the treatment of chronic wounds, drug delivery, and tissue engineering [20–22]. Carboxyethyl chitosan (CEC), a water-soluble derivative of chitosan, is biocompatible, biodegradable, moisturizing, antibacterial, and antioxidant [23,24]. Similar to CEC, oxidized sodium alginate (OSA) is a hydrophilic and biodegradable anionic natural polysaccharide with a relatively low cost, which can be applied in various biomedical applications [25,26]. The OSA solution can be easily cross-linked through the exchanging of the Na^+ in the carboxylate groups of OSA with divalent cations (e.g., Ca^{2+}) and the Schiff-base reaction between aldehyde groups of OSA and amine groups to form ionic and imine cross-links, respectively [27]. Wei et al. [28] developed a self-healing hydrogel based on OSA and CEC and investigated its compatibility in contact with NIH 3T3 cells. However, the adhesive and antibacterial properties of this hydrogel were not investigated for wound healing application. Cao et al. [29] also prepared hydrogels based on carboxymethyl chitosan (CMC), gelatin, and OSA with low adhesion strength (11 kPa). In another study, CEC-OSA hydrogel was introduced as a novel injectable carrier to deliver neural stem cells and treatment of neurological disorders [30]. Zhang et al. investigated the role of blueberry anthocyanins (BA) on the antioxidant and anti-inflammatory properties of hydrogels based on carboxymethyl chitosan and oxidized hyaluronic acid. They reported that BA and hydrogels exert synergistic effects in promoting wound healing. Güngör and Ozay [31] studied the color changes in the acrylate derivative (BTBm) of bromothymol blue in different pH environments and proposed that they could be used as a pH-sensitive smart wound dressing. In other work, mesoporous polyester beads containing brilliant yellow dye were embedded in the hydrogel microfibers based on alginate and glycerol [9]. During this process, the response time and sensitivity of pH-sensitive fibers with different compositions and thicknesses were investigated and indicated that they could be used as a care device for monitoring the wound healing process. Nevertheless, none of the colorimetric pH-responsive, bioadhesive, hemostatic, cytocompatibility, and antibacterial properties were simultaneously studied in these self-healing hydrogels.

Silver nanoparticles (Ag NPs) have been used extensively for their antibacterial properties, low-cost, and high biocompatibility in the production of wound dressings [32]. However, the antibacterial and anti-biofilm properties of Ag NPs are severely limited because of their ease of agglomeration and oxidation. As a result, Ag NPs have been physically or chemically modified and functionalized to ensure their antibacterial properties [33,34]. In our previous work, we synthesized a novel colorimetric pH indicator using silver-tannic acid nanoparticles (Ag-TA NPs), which were modified with various concentrations of red cabbage (ATR NPs) [35]. Plant extract-derived Ag NPs like polyphenols of tannic acid (TA) as surface modifiers are more preferable to microorganism-derived NPs. TA is non-toxic and inexpensive and, due to its antimutagenic, anticarcinogenic, and antioxidant properties, can be exploited as a chelating agent for a variety of inorganic cations [36]. These polyphenols coated on the surfaces of Ag NPs could not only provide a reactive layer on the NPs' surface for electrostatic and hydrophobic interactions but also, due to having plenty of hydroxyl groups, could increase the material's adhesiveness for tissue adherence. The ATR NPs showed significant antibacterial properties against *Escherichia coli (E. coli)* and *Staphylococcus aureus (S. aureus)* as well as high cytocompatibility in contact with fibroblast cells.

Our current work aims to develop pH-sensitive hybrid hydrogel-based adhesives composed of CEC-OSA (CAO), containing different concentrations of ATR NPs. The hybrid hydrogel is referred to as CAO/ATR. We hypothesize that incorporating modified Ag NPs containing TA and the natural dye of red cabbage into the hydrogel network would show the expected adhesive and antibacterial properties, as well as pH-responsiveness. The effects of ATR NPs on physical and chemical properties, swelling and mass loss, self-healing, and adhesive properties of hydrogels are examined. Furthermore, the antibacterial properties against *E. coli* and *S. aureus*, cytocompatibility, and blood compatibility are also evaluated in order to examine the positive effects of hybrid hydrogel in the treatment of skin wounds.

2. Materials and method

2.1. Materials

Sodium alginate, chitosan, adipic acid dihydrazide (ADH), and ethylene glycol were purchased from Sigma-Aldrich (USA). Silver nitrate ($AgNO_3$), sodium periodate ($NaIO_4$), acrylic acid, hydrochloric acid (HCl), and sodium hydroxide (NaOH) were obtained from Merck (Germany). Fresh red cabbage (RC) was purchased from a local supermarket. All agents were used without further purification.

2.2. Synthesis of oxidized sodium alginate (OSA)

The OSA was synthesized as previously described with appropriate modifications [28,37]. Briefly, 5 g of sodium alginate was dissolved in 25 ml of water and stirred for 1 h. Then, 0.5 g of $NaIO_4$ was added to the solution and agitated for 5 h at 20 °C in the dark. To quench unreacted periodate, 5 ml of ethylene glycol was added at the end of the reaction and agitated for 30 min. The reaction solution was subsequently dialyzed for three days against deionized water in a dialysis tube (cut off $M_w = 12$, 000–14,000 Da), followed by one day of lyophilization.

2.3. Synthesis of carboxyethyl chitosan (CEC)

CEC was prepared as previously described with appropriate modifications [38]. Briefly, 1 g chitosan was added to 50 ml of deionized water containing acrylic acid (1.46 ml) and continuously stirred at 50 °C for 3 days. Afterward, the NaOH solution (1 M) was added to the reaction mixture to bring the pH up to 10–12, allowing the COOH to be converted to COO–Na^+. The mixture was subsequently dialyzed for 3 days in a dialysis tube (M_w = 12,000–14,000 Da) against deionized water, followed by lyophilization for one day.

2.4. Preparation of CAO/ATR hybrid hydrogels

For the preparation of hybrid hydrogels, 2 wt% CEC and 4 wt% OSA solutions were separately prepared in deionized water. Subsequently,

ADH (8 wt% related to the total weight of polymers) and $CaCl_2$ (4 wt% related to the total weight of polymers) were added to the CEC solution. To prepare ATR NPs, the colloidal suspension of Ag-TA NPs was treated with 50 (v/v)% RC, according to our previous work [35]. Different concentrations of ATR (0.5, 1, 2, and 3 wt%) were added to the OSA solution and sonicated (20 kHz, 60 W) for 10 min. Finally, the obtained mixtures of CEC and OSA/ATR were thoroughly mixed by vortexing until the homogeneous hydrogels were obtained. The hydrogels were named CAO/ATR-0.5, CAO/ATR-1, CAO/ATR-2, and CAO/ATR-3, according to the concentration of ATR NPs. CAO hydrogel was similarly synthesized and used as a control.

2.5. Physiochemical properties

The surface charge and size distribution of ATR NPs were measured by zeta potential analysis and Dynamic light scattering (DLS, HORIBA Scientific SZ-100 V2, Japan). Moreover, the hybrid hydrogels were lyophilized for 24 h before characterization. The morphology of nanoparticles was also investigated using transmission electron microscopy (TEM, Philips CM 120, Netherlands) with an accelerating voltage of 100 kV. Fourier transform infrared (FT-IR) spectroscopy (Tensor27, Bruker, Germany) was used to investigate different functional groups of the modified Ag NPs (Ag-TA and ATR NPs) and lyophilized CAO/ATR hybrid hydrogels. A scanning electron microscope (SEM, Phillips XL 30, Netherlands) and Field emission-scanning electron microscope (FE-SEM, QUANTA FEG-450, FEI company, US) equipped with energy dispersive X-ray (EDX) analysis were used to analyze the morphology and internal structure of the hydrogels and nanoparticles, respectively. X-ray diffraction analysis (XRD, Philips X'PERT MPD, Germany) was used to identify the crystal structure of ATR NPs in the hydrogel matrix.

2.6. Weight loss and swelling behavior of hydrogels

To investigate the role of ATR NPs on the swelling degree of hydrogels, the cylindrical hydrogels (5 mm D, volume: 150 μl; n = 3 for each group) were freeze-dried and weighed. The dry samples were incubated in phosphate buffer solution (PBS, pH 7.4) at 37 °C for 90 min. The swollen hydrogels were taken out at a predetermined time, superficially dried with tissue paper, and immediately weighed. The swelling percentage (%S_t) of the hydrogels at each time was calculated according to formula 1 [39].

$$\%S_t = \frac{(W_t - W_0)}{W_0} \times 100 \quad (1)$$

where W_0 and W_t denote the initial mass of the dry hydrogel and the mass of wet hydrogel at the time point, respectively. The findings were plotted as %S_t (average %S_t at each time with standard deviation) vs. time.

To investigate the role of ATR NPs on the mass loss of samples, the cylindrical disks (10 mm D × 5 mm H) were lyophilized and then immersed in 2 ml of PBS solution. Then, the samples were incubated in PBS solution at 37 °C for a predetermined time (2, 5, 8, and 12 days). After being taken out from PBS, the residual hydrogels were rinsed with deionized water, lyophilized, and weighed. The mass loss of hydrogels was determined according to the following formula [40]:

$$\text{Weight loss}\% = \frac{(W_0 - W_t)}{W_0} \times 100 \quad (2)$$

where W_0 and W_t denote the weight of the dried hydrogels before and after incubation, respectively.

2.7. Water vapor transmission rate of hydrogels

To determine the moisture permeability of the hybrid hydrogels, the water vapor transmission rate (WVTR) was measured according to the standard of the American Society for Testing and Materials F 1249 [41]. Briefly, hydrogel samples were cut into circular pieces with a thickness of 1 mm and diameter of 16 mm and were put on the mouth of a bottle with an inner diameter of 15 mm containing 15 ml distilled water and were sealed with Teflon tape on the bottle mouth. An empty bottle without covers was considered a control. Then, the bottles were placed into an incubator with a constant temperature of 35 °C and relative humidity of 35–45%. Bottles were removed after 24 h and weighed again. WVTR ($g.m^{-2}.day^{-1}$) was calculated according to Eq. (3):

$$\text{WVTR}\ \left(g.m^{-2}.day^{-1}\right) \frac{W_i - W_f}{A} \times 100 \quad (3)$$

where, A is the permeation area of samples, and W_i and W_f are the initial and final weight of bottles, respectively. All trials were performed in duplicate.

2.8. Mechanical properties

To examine the compressive mechanical properties, the cylindrical-shaped hydrogels (10 mm D × 10 mm in H) were prepared. Hydrogels were compressed using a Hounsfield H25 KS instrument with a compressive strain rate of 1 mm min^{-1} and 50 N preloading. In addition, the rheological characteristics of the cross-linked hydrogels were determined at 37 °C using a rheometer (Anton Paar MCR 502) with a plate-plate geometry (25 mm diameter) and 1 mm gap. A dynamic frequency sweep was performed with an angular frequency of 1–10 rad s^{-1} and a shear amplitude of 1%. The strain sweep test was from 0.1% to 800% with a constant angular frequency of 1 rad s^{-1}. In addition, the viscosity of the hydrogels obtained from the shear rates varied from 0.1 to 100 s^{-1}. Furthermore, cyclic compressive tests of CAO and CAO/ATR-1 were performed at a rate of 1 mm/min until 50% of strain, without resting time between each cycle. The toughness and energy dissipation of hydrogels during the cycle were also calculated by determining the area between the loading and unloading cycle of curves. After the 5th cyclic test, the specimens were lyophilized for 24 h and their morphology was investigated by SEM.

2.9. Self-healing ability

The self-healing ability of the optimized hybrid hydrogel was evaluated using macroscopic self-healing tests. Two disk-shaped hydrogels were prepared; one of them was stained with rhodamine B. These two hydrogels were cut into two pieces. Then, two pieces of alternate colors were combined to reform an integral blended hydrogel disk and were maintained at 25 °C for 3 h. Finally, the healed hydrogel disks were suspended under gravity and then immersed in PBS (pH 7.0) to check their stability [28]. In addition, the self-healing capacity of hydrogels was assessed using an alternate-step strain sweep test at a constant frequency of 1 rad s^{-1}. The oscillatory strain was switched between a small strain (γ = 1.0%) and a large strain (γ = 300%), ensuring a duration of 120 s for each strain value, and three cycles were carried out [42].

2.10. pH-sensitivity

The pH sensitivity of the CAO/ATR hydrogels was investigated upon exposure to sodium acetate buffer (pH = 3–5) and phosphate buffer solutions (pH = 6–9). During this process, different pH values were adjusted by adding HCl (1 M) and NaOH (1 M). The buffer solutions with different pH values of 3, 4, 5, 6, 7, 8, and 9 were prepared and kept at 5 °C for further use. Typically, the disk-shaped hydrogels were first split into four pieces and then immersed into 3 ml of each buffer solution for 10 min. The hydrogels were imaged using the phone camera for the smartphone-based analytical measurement. Because of the variable brightness of the ambient environment, chromatic aberration was applied between the color of an image captured with a smartphone and

the real color of the object [43].

2.11. In vitro adhesion test

Based on ASTM F2255-05, lap-shear tests were carried out on the cow skin to determine the adhesive properties of CAO and CAO/ATR-1 hydrogels [29]. The fresh cow skins were cleaned by removing subcutaneous fats and hairs and then washing them under running water with detergent. The skins were sliced into 2 × 2 cm squares and glued on a metal sheet. 200 μl of CAO and CAO/ATR-1 (n = 3) hydrogels were poured on top of the smooth skin. After that, the two pieces of skin were brought into contact with each other. Then, the smeared region of the two cow skin sheets was pressed with a 100 g weight and incubated at 25 °C for 2 h. The adhesion strength of the hydrogels was determined using the shear test under a 50 N load and at a rate of 10 mm min^{-1}.

2.12. Antibacterial activity

The antibacterial activity of hybrid hydrogels was studied using the disk diffusion method against *E. coli* and *S. aureus*. In brief, 50 μl of standard microbial suspension (10^8 cfu ml^{-1}; according to 0.5 McFarland turbidity standards) was spread on an agar petri-dish and incubated for 10 min at room temperature. Then, circular wells with a diameter of 0.5 mm were created on the surface of the solidified agar. Then, 100 mg of each sample was injected into the wells. The dishes were incubated at 37 °C for 24 h in order to measure the inhibition zone. Tetracycline was used as the positive control, and sterilized distilled water was used as the negative control.

2.13. In vitro blood-hydrogel interaction

The hydrogel-blood interaction was studied using the blood clotting index (BCI) and hemolysis assays [44]. The fresh blood from an adult volunteer was provided in a vial containing an anticoagulant (3.8 wt% sodium citrate). The hydrogel samples were immersed in a water bath for 5 min at 37 °C to adjust their surface temperature before considering the BCI value. After that, 270 μl of the prepared blood (0.3 ml of whole blood containing 0.024 ml of $CaCl_2$ solution (0.2 M)) was slowly poured over the hydrogels to cover them. After 10 min incubation, deionized distilled water (DDW, 10 ml) was carefully added to the hydrogels without damaging the blood clot. Following centrifuging the separated solutions for 30 s at 2500 rpm, the supernatants were combined with DDW (40 ml) and maintained at 37 °C for 60 min. Subsequently, the absorbance (abs) of the solutions was measured at 542 nm using UV–vis spectroscopy. Furthermore, blood absorbance (250 μl in 50 ml DDW) was measured as a control. Finally, the BCI value was calculated by the following formula.

$$\text{BCI index} = \frac{(abs\ of\ blood\ in\ contact\ with\ sample\ at\ 542\ nm)}{(abs\ of\ whole\ blood\ at\ 542\ nm)} \times 100 \quad (4)$$

The hemolysis ratio (HR) was also studied to assess the blood compatibility of hydrogels. The hydrogels were washed in sequential order with DDW and normal saline solution. Following adding 10 ml of saline solution to the samples, they were incubated at 37 °C for 60 min. The hydrogels were then inoculated for 60 min with 0.2 ml of diluted whole blood (8 ml of whole blood in 10 ml of normal saline solution). The solutions were collected and centrifuged at 2500 rpm for 5 min. Finally, the supernatant absorbance at 542 nm was determined by a UV–vis spectrophotometer, and the HR was calculated based on formula 5.

$$\text{HR} = \frac{(AS - AN)}{(AP - AN)} \times 100 \quad (5)$$

In this equation, AS, AP, and AN are the absorbance of supernatant, positive (0.2 ml of diluted whole blood mixed with 10 ml of DDW), and negative (0.2 ml diluted whole blood with 10 ml of normal saline) control, respectively.

2.14. Cell culture

The cytotoxicity of hydrogels was examined using L929 fibroblast cells (passage number 17). The hydrogel disks (n = 3) with the dimension of 10 mm D × 2 mm H were sterilized under the clean bench after exposure to UV light for 20 min, followed by the cell seeding with a density of 10^4 cells/well on the samples and tissue culture plate (TCP, control) at 37 °C and 5% CO_2. The culture medium was composed of Dulbecco's Modified Eagle's medium (DMEM, Gibco) supplemented with 10% fetal bovine serum (Bioidea) and 1% streptomycin/penicillin (Gibco). The 3-(4,5-dimethylthiazol-2-yl)-2,5-diphenyl tetrazolium bromide (MTT) assay was used to measure the cell proliferation rate on the hydrogel samples. MTT solution (0.5 mg/mL in PBS) was added to cell-seeded samples and control after 1, 3, and 5 days of culture. As a result, the formazan crystals were decomposed in dimethyl sulfoxide (DMSO, Merck), and the optical absorption was determined at 490 nm using a microplate reader (Biorad Instruments). Ultimately, the normalized proliferation rate to the control was calculated as follows.

$$\text{Normalized proliferation rate}\ (\%) = \frac{A_s - A_b}{A_c - A_b} \times 100 \quad (6)$$

in which A_S, $A_{b,}$ and A_c are introduced as the absorbance of the sample, blank (DMSO), and control (TCP), respectively.

Furthermore, the viability of the cells in contact with hybrid hydrogels with various compositions was measured using Live/Dead assay based on Calcein AM/ethidium homodimer-1 (EthD-1) kit (Biotium, UK). According to the manufacturer's protocol, after 1 and 5 days of culture, 100 μl of Calcein AM/EthD-III solution was added to cover the cell-seeded samples and left at 37 °C for 20 min. After rinsing the samples using PBS, an inverted fluorescence microscope (Nikon TE 2000-U, Japan) was used to take images. The number of live cells (green cells) and dead cells (red cells) was estimated using ImageJ software, and the cell viability was computed by dividing the live cells by the total cell number (n = 3).

The role of ATR NPs on the cytoskeletal organization (F-actin) of fibroblasts was further investigated using phalloidin/DAPI staining. At 3 and 5 days of culture, the cell-seeded hydrogels were fixed using 3.7% (v/v) paraformaldehyde (Sigma-Aldrich) solution and subsequently permeabilized for 5 min with Triton 100x. After rinsing with PBS, the samples were incubated with rhodamine Phalloidin solution for 30 min. Then, a 6-diamidine-2-phenyl indole dihydrochloride (DAPI, Sigma-Aldrich) solution was added to the samples for 5 min. Finally, the samples were imaged with a fluorescence microscope. The morphology of fibroblasts seeded on the hydrogels was also analyzed using the SEM. After 3 days of culture, the cells were fixed with 3.7%(v/v) paraformaldehyde (Sigma-Aldrich) for 20 min at room temperature. After two times rinsing with PBS, the cell-seeded hydrogels were dehydrated in the graded concentrations of ethanol (50, 70, 80, 90, and 100 (v/v) %) for 5 min, at 4 °C, respectively. After freeze-drying, the samples were imaged using SEM.

2.15. Statistical analysis

All measurements were conducted in at least triple samples, and the data were expressed as mean ± standard deviation (SD). Statistical analysis in the measurement was carried out by one-way ANOVA analyses, using GraphPad Prism Software (V8).

3. Result and discussions

3.1. Physicochemical characterization of CAO/ATR hybrid hydrogel

Before the synthesis of hybrid hydrogels, CEC, OSA, and ATR NPs were synthesized. FE-SEM image of ATR NPs, presented in Fig. S1A, revealed the formation of non-spherical NPs with irregular shapes with a

mean size of 134 ± 24 nm. TEM image was used to determine the shape and size of ATR NPs (Fig. S1Bi). The particle size distribution is presented as a histogram after measuring at least 100 NPs. The TEM image shows the formation of dispersed spherical particles and the mean particle sizes of 8.7 ± 3.7 nm with a narrow size distribution for ATR NPs. The mean size of the NPs was lower than the sizes obtained from SEM and DLS, which is mainly attributed to the comparatively high resolution and accuracy of TEM. Particles are not agglomerated which supports the monodispersity and colloidal stability of ATR NPs. EDX analysis in Fig. S1C also demonstrated that due to surface plasmon resonance, the characteristic signals of the silver element in the range of 2.6–3.4 keV, were detected, confirming the formation of silver nanoparticles [45]. The presence of O and C signals was also due to the adsorbed phenolic compounds on the surface of AgNPs. In addition, according to DLS analysis (Fig. S1D), the hydrodynamic size of ATR was estimated at 75 ± 14 nm with a polydispersity index (PDI) of about 0.23, confirming that the particle population was nearly monodispersed. Moreover, owing to adsorbed polyphenolic and anthocyanin compounds as well as dissociated functional groups present in the nanoparticle structures, the zeta potential of ATR NPs (Fig. S1E) was estimated at about −19.3 ± 2.0 mV.

According to Fig. 1A, the CAO hydrogel consists of an imine network including extensive reversible Schiff-base units between amine and aldehyde groups, and a chelate reaction between calcium ions and carboxylic acid groups of OSA. $NaIO_4$ oxidized the vicinal diol groups of sodium alginate to aldehyde. Chitosan is also converted to CEC with water solubility in the presence of acrylic acid. The aldehyde groups of OSA react with the amine groups in CEC and ADH to form Schiff-base and acylhydrazone bonds in the hydrogel networks. ADH reacts with carbonyl groups in the CEC to enhance amine content, decreasing the CEC's helical shape and serving as a secondary cross-linker. Additionally, the Ca^{2+} ions form a physical bonds (chelating network) with the carboxylic acid groups on the OSA chain, thereby accelerating the gelation of hydrogels. ATR NPs are dispersed between polymer chains via hydrogen bonds and created multiple non-covalent bonds, which form stable and reversible physical cross-linking in the polymer chains. FTIR

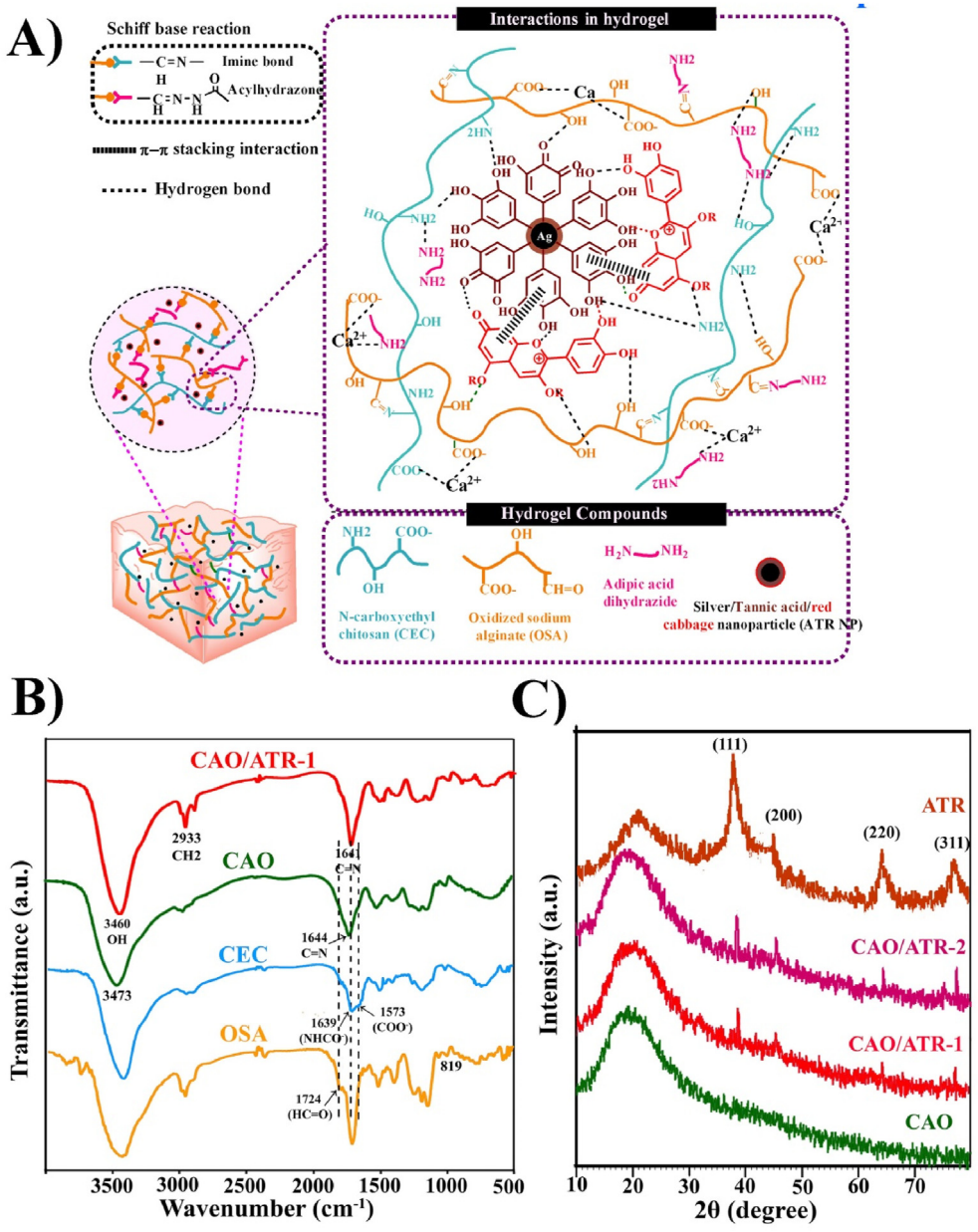

Fig. 1. (A) Schematic model of the interactions within CAO/ATR hydrogel network, (B) FTIR spectra, and (C) XRD patterns of CAO/ATR hydrogels.

spectra were utilized to better understand the basic structures of OSA, CEC, and CAO. According to Fig. 1B, the weak symmetric vibration peak at 1724 cm^{-1} revealed the presence of the aldehyde group in the OSA. Furthermore, the OSA showed a reduced intensity of absorptions at 819 cm^{-1}, compared to sodium alginate [46], which could be related to the breakage of the C–O–C on the alginate chains after oxidation by $NaIO_4$ [47]. In the CEC spectrum, there are absorption peaks at 1568 cm^{-1}, and 1644 cm^{-1}, which were ascribed to the asymmetrical stretching vibrations of COO^- and amide (−NHCO) groups [38]. The new wide peak in the spectrum of CAO hydrogel (1639 cm^{-1}, N = C) corresponds to the imine bond of the Schiff-base reaction, followed by the decreased carboxyl peak in CEC and the absence of an aldehyde peak in OSA. These findings suggested that the hydrogel was successfully cross-linked through the Schiff-base reaction. For ionic interactions, typically the stretching vibration of COO- downshifts from 1568 cm^{-1} to 1553 cm^{-1}, as a result of the coordination of the COO- groups of OSA and CEC to calcium ions in the bidentate mode. However, due to the overlapping of absorption peaks in the CAO hydrogels, this could not be determined [48, 49].

After the addition of ATR NPs within the CAO hydrogel, polar groups in the hydrogel structure (hydroxyl, amine, and carbonyl groups) could attract ATR NPs containing TA via electrostatic interaction and hydrogen bonding. Therefore, the NPs were well-dispersed within the polymer network, which may lead to homogenous properties of the hydrogel. In addition, after the incorporation of ATR NPs, the peak at 1641 cm^{-1} (Fig. 1B) becomes more pronounced. This might be due to the presence of aromatic groups on the surface of the nanoparticle. Compared to the CAO hydrogel, CAO/ATR-1 hybrid hydrogel showed no additional peak. It might be due to the lower concentrations of ATR NPs in CAO hydrogel [50].

The XRD patterns of CAO, ATR NPs and CAO/ATR-1, and CAO/ATR-2 are also presented in Fig. 1C. XRD pattern of ATR NPs consisted of five diffraction peaks at $2\theta = 38.10°$, 44.20°, 64.41°, 77.39°, and 81.8°, which corresponded to the diffraction of the (111), (200), (220), (311), and (222) crystallographic structures of the face-centered cubic (fcc) of silver, respectively (JCPDS File NO. 04–0783). No further peaks corresponding to any undesirable impurity phases were detected [51]. Compared to the CAO pattern, the incorporation of the ATR NPs resulted in the formation of relatively strong peaks at $2\theta = 38.10°$, 44.20°, 64.41°, and 77.39° with an enhanced intensity after the addition of a higher concentration of ATR NPs. These peaks contributed to the characteristic peaks of Ag, presented in the hydrogel matrix. SEM images were used to analyze the cross-sectional morphology of the CAO/ATR hydrogels (Fig. 2A). All hydrogels had a continuous and porous structure, which resulted from the development of ice crystals during the freeze-drying process. However, between hydrogels, the CAO/ATR-1 and CAO/ATR-2 hydrogels revealed dense structures. According to Fig. 2B, with increasing ATR NPs content upon 2 wt%, the average pore diameters in hydrogels were significantly decreased from 248 ± 65 μm to 65 ± 17 μm. It might be due to the physical cross-linking bonds between the ATR NPs containing TA and the polymer chains that form a dense network topology. However, incorporating more ATR NPs (3 wt%) enhanced the average pore size (101 ± 61.4 μm) of hybrid hydrogels. Moreover, the pore morphology was not uniform compared to the other hydrogels, which could be attributed to the high concentration of nanoparticles and local excess noncovalent cross-linking caused by the short reaction time [29]. In a similar study, Zhang et al. [52] found that the pore size of hydrogels decreased after the incorporation of ZnO NPs. In other studies, Kong et al. [37] demonstrated that the average pore diameter of hydrogels decreased with the increase of OSA concentration

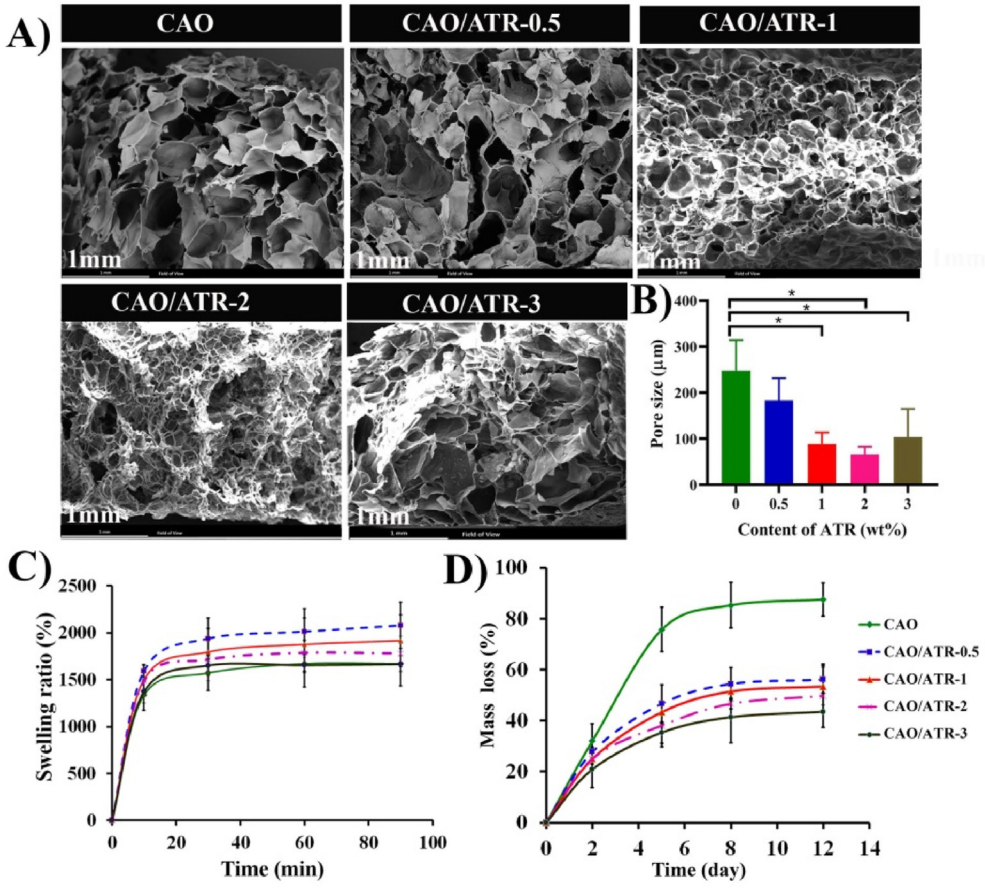

Fig. 2. (A) SEM images and (B) average pore diameters of CAO/ATR hydrogels (*: $p < 0.05$). (C) Swelling ratio, and (D) Mass loss of CAO/ATR hydrogels during soaking in PBS.

in CEC/OSA/CuS hydrogels. The mechanical performance of porous materials is strongly influenced by pore structures. The compact construction with smaller pore sizes can improve the compressive strength of hydrogels. It has been shown that establishing hydrogen bonding and chemical linkages via cross-linking between functional groups improves the mechanical strength of porous scaffolds [42,53]. As a result, the CAO/ART-1 and CAO/ATR-2 are expected to show improved compressive strength. In addition, hydrogels with porous structures allow higher perfusion of nutrients and oxygen within the hydrogel protecting the flourishing of cells [54].

The changes in the inner morphology of hybrid hydrogels have influenced the swelling ratio and the mass loss of hydrogels. As depicted in Fig. 2C, all hydrogels had a similar swelling ratio after 90 min. The swelling level enhanced rapidly in the first 15 min and afterward plateaued at a relatively constant swelling level. Therefore, the swelling ratio was measured till 90 min, as similarly reported in previous studies [36]. Notably, the swelling ratio of CAO/ATR-0.5 (2078% ± 244%) increased dramatically compared to CAO hydrogel (1671% ± 237%), followed by a progressive decrease in the swelling ratio of the hybrid hydrogels, with increasing ATR NPs content. This behavior could be due to the presence of an abundant amount of –OH groups on the surface of TA in the ATR NPs, which increased affinity for water adsorption. By increasing the ATR NPs concentration, a compact network structure with high cross-link density and a small mesh size was formed between polymer chains and ATR NPs via physical interactions (e.g., hydrogen bonding, -stacking, and ionic bonds) that would hinder water diffusion into the hydrogel network. On the other hand, more ATR NPs in the hydrogels would occupy more space that should be filled by water, therefore, resulting in a lowering of the swelling rate. This conclusion was in agreement with the findings provided by Ma et al. [54]. The high porosity and swelling ratio of the CAO/ATR hydrogels could be advantageous for absorbing the wound exudation and creating a moist environment for wound healing [55].

Controllable mass loss over time is a fundamental requirement for polymeric hydrogels in bioadhesive applications. Hence, the CAO and hydrogel hybrids were incubated in a PBS solution, and their weight changes were used to analyze their mass loss. According to Fig. 2D, the rate of the weight changes of the hydrogels was significantly dependent on the content of ATR NPs under the same experimental conditions. The CAO and CAO/ATR (0.5, 1, 2, and 3) hydrogels showed a rapid mass loss in the first 5 days, which was lowered in 12 days from 87.5 to 43.5% with the increase of the ATR nanoparticle content. In general, hydrogels' chain integration and swelling ratio had a direct impact on how quickly the mass of the hydrogels was changed. Based on our study, the inclusion of ATR NPs in the hydrogel structure reduced water absorption by forming hydrogen bonds with the hydrogel chains, increasing the stability of the hydrogel in the hybrids [46,56]. Tavakoli et al. [44] also indicated that the incorporation of ZnO/polydopamine nanoparticles into methacrylated Kappa-carrageenan hydrogel noticeably reduced the degradation rate compared to the pure hydrogel.

According to the literature, the average WVTRs for normal skin, first-degree burns, and granulating wounds are 204, 279, and 5138 g m^{-2}.day^{-1}, respectively [57]. The WVTR of the dressing should be neither too low nor too high, since a low permeability may cause the accumulation of the exudates and result in leakage, whereas a high permeability may lead to excessive dehydration of the wound area. It has been suggested that the WTVR for a good wound dressing should be in the range of 2000–2500 g m^{-2}.day^{-1}, which can maintain a proper moisture level on the wound without dehydration [58]. Most dressings can be preserved on the wound for up to 7 days, but this varies according to the amount of exudates [59]. Our results confirmed that the incorporation of ATR NPs decreased the WVTR value due to the decreased pore size of the hybrid hydrogels. The WVTRs of CAO and CAO/ATR are 2953 ± 7 and 2248 ± 5 g m^{-2}.day^{-1}, respectively. Thus, CAO/ATR-1 was suitable for wound dressings as it would prevent the dryness of the wound and loss of water, while preventing exudate formation in the wound bed, thus decreasing the risk of contamination. Also, it can provide a moist environment for a good response to changes in the wound's pH.

3.2. pH-sensitivity of CAO/ATR hybrid hydrogel

The pH sensitivity of CAO-ATR-1-based hydrogels was investigated using various characterization methods. At first, hydrogel formation of CAO/ATR-1 in environments with varying pH such as acidic, basic, and neutral was investigated. At neutral pH, the hydrogels were formed in 3 min, while at basic pH they formed after 6 min. The hydrogel formation with increasing pH was delayed; however, at a low pH (acidic), no hydrogelation was observed even after 24 h. These results suggested that the pH of the solution played an important role in imine bond formation between aldehyde groups in OSA and amine groups in CEC and ADH. Before hydrogel formation, when the H^+ concentration was too high, the amino groups were protonated, and the nucleophilic attack occurred too slowly to inhibit the formation of the imine bond, leading to the reaction's inefficiency. Therefore, Schiff-base formation and gelation were accelerated under neutral conditions.

The visible color changes of the wound dressings containing natural pigment respond to a wide range of pH changes. They can inform doctors and patients to assess the wound healing condition and alarm the bacterial infection. Encapsulation of the ATR NPs within the CAO hydrogel not only ensures that the colorimetric indicator NPs do have contact with the skin and disperse within the wound site but also it prevents the dye from leaching out of the hydrogel onto the skin [11,60]. The effect of the changes in the pH of buffer solutions on the color changes of anthocyanin incorporated into the bioadhesive hydrogels of CAO/ATR is presented in Fig. 3A. There were no visible color changes in CAO hydrogel in the pH range of 3.0–9.0, owing to the lack of anthocyanins. In contrast, the CAO/ATR hydrogels were sensitive to all buffers tested and resulted in color variations, ascribed to the structural transformation of anthocyanins. CAO/ATR hydrogels were initially red, and the color gradually changed to green with an increase in pH from 3.0 to 9.0, Fig. 3A. It is noteworthy that the color response to the pH change of the CAO/ATR hydrogels differed from that of the anthocyanin solution [61]. It was suggested that anthocyanin involved the interactions with CAO and ATR and thus could not show further structural transformations with increasing pH [62]. The red color was assigned to the flavylium cation, which was enhanced when anthocyanin was in a strongly acidic medium (Fig. 3B). With a further increase in pH, the rapid hydration of flavylium cation's generated colorless species of carbinol pseudo-base and chalone. As a result, the red color intensity decreased. In the alkaline pH range, the quinoidal anhydrobase was formed due to deprotonation of the flavylium cation, which exhibited a green hue at pH 7–8 [63].

Mirani et al. [64] also prepared 3D-printed alginate fibers that were encapsulated with mesoporous resin beads doped with a pH-responsive dye (brilliant Yellow or cabbage juice). They indicated antibacterial properties in the presence of antibiotics (gentamicin). However, their application in wound healing was limited due to their poor mechanical properties, lack of self-healing, and lack of adhesiveness to the skin [64]. Lee et al. [65] also reported a pH-sensitive colorimetric hydrogel based on catechol-conjugated alginate loaded with pyrocatechol violet dye. The results showed that the color change of the hydrogel was weak between pH 2 and 7. Therefore, it could be more suitable for detecting a strong acid or base than for monitoring a weakly acidic or neutral solution. Arafa et al. [66] also designed a transparent, soft, and pH-sensitive wound dressing with hydroxyethyl cellulose combined with Curcuma Longa extract. Hydrogel matrices on cotton gauze and submerged in various pH buffer solutions revealed distinct color changes, ranging from clearly yellow for pH $\leq$ 7 to dark red for pH $>$ 7. Compared to the literature, CAO/ATR hybrid hydrogels are able to preserve wound moisture, have a low cost of production, are easy to process, and are pH-sensitive.

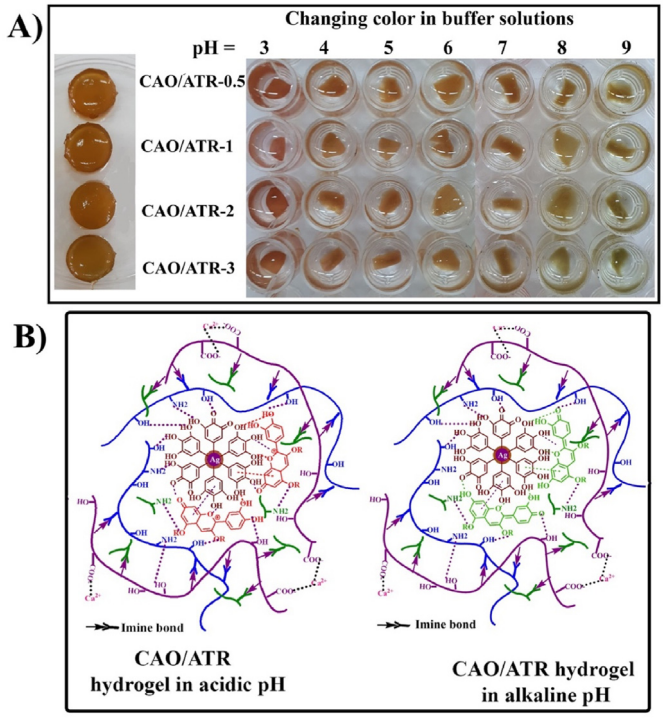

Fig. 3. pH sensitivity of CAO/ATR hydrogels: (A) Color change of hybrid hydrogels at different pH values, (B) Schematic illustration of pH-dependent chemical structures of anthocyanin in acidic and basic media. (For interpretation of the references to colour in this figure legend, the reader is referred to the Web version of this article.)

3.3. Mechanical and rheological performance of CAO/ATR hybrid hydrogel

Mechanical properties of the CAO and CAO/ATR hybrid hydrogels were examined by compression tests. The typical stress-strain curves of CAO and hybrid hydrogels are illustrated in Fig. 4A. The curves exhibited a linear region at initial strains <30% and a region with an increasing slope at strains 30–70%. The compressive strength and compressive modulus extracted from the stress-strain curves are presented in Fig. 4B and C. According to Fig. 4B, the CAO hydrogel showed the lowest compressive strength among all hybrid hydrogels. Increasing ATR NPs content up to 1 wt% has resulted in enhancing the compressive strength of the CAO matrix from 35.1 ± 2.1 kPa to 97.5 ± 2.9 kPa. It must be noted that with further addition of ATR NPs up to 3 wt%, the compressive strength decreased to 62.5 ± 3.8 kPa. A similar result was reported by Wang et al. [67], who fabricated hydrogel/microsphere composites. CAO/ATR-1 also showed a significantly higher compressive modulus (28.3 ± 1.1 kPa) than other hydrogels ($P < 0.05$) (Fig. 4C), which were comparable to human skin [68,69]. The improved mechanical performance of CAO with increasing ATR NPs could be due to the strong electrostatic and intramolecular and intermolecular hydrogen bonding between the active groups of CAO and ATR NPs, resulting in the molecular chain entanglement, which might limit the deformation of the polymer molecular chain under external strain. During the compression process, a portion of the force was passed to the nanoparticles distributed in the hydrogel, leading to an increased compressive strength (Fig. 4D). Also, the presence of NPs in the hydrogel can cause a significant deviation in crack propagation in the matrix, which increases the fracture toughness. After the compression test, the fracture surface of CAO/ATR-1 was imaged using SEM (Fig. 4E) showing the pores containing some irregular stretched filaments interconnecting with the CAO matrix. These

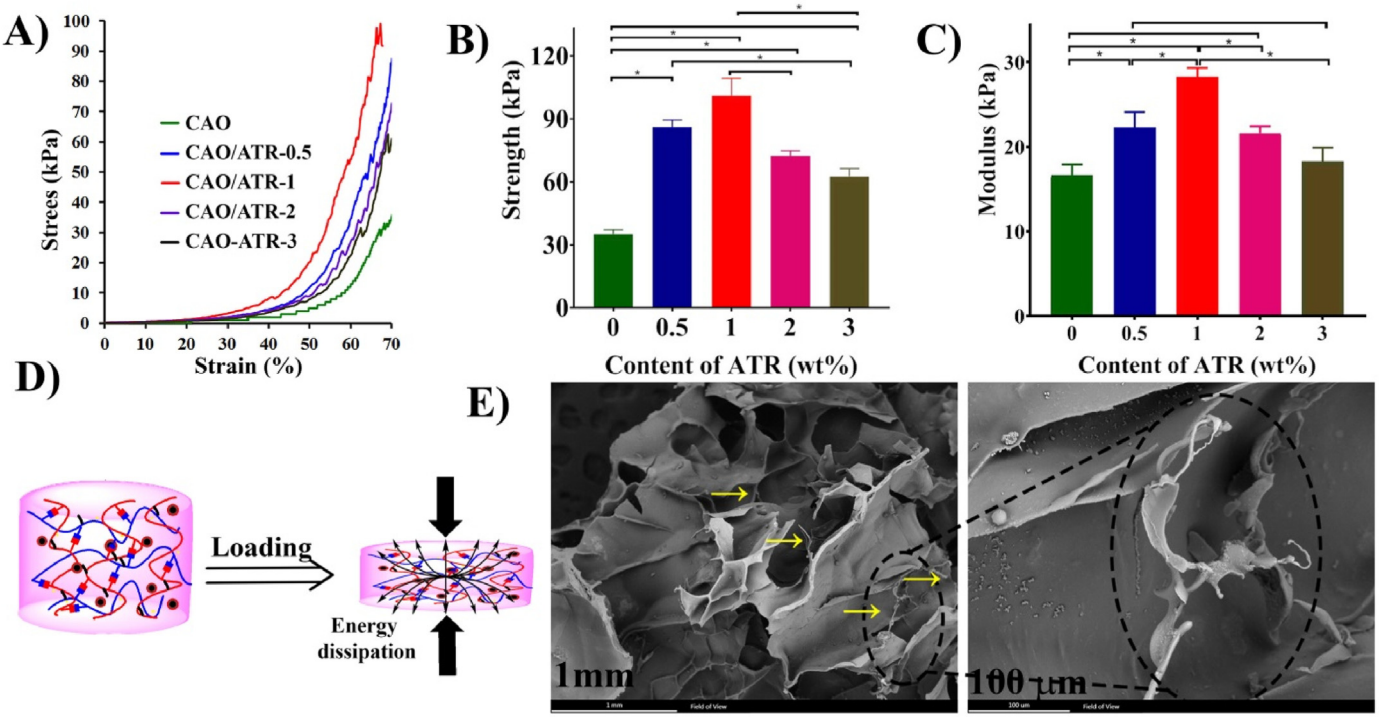

Fig. 4. Mechanical properties of CAO/ATR hydrogels containing various concentrations of ATR: A) The compressive stress-strain curves, B) compressive strength, and C) compressive modulus at 70% strain (*: $p < 0.05$). D) Schematic of the compression behavior of CAO/ATR hybrid hydrogel. E) SEM images after the compressive test.

filaments might be attributed to the presence of TA in ATR, which provided a toughening function between polymer chains to absorb and dissipate energy. These filaments weren't clearly visible prior to the compressive test due to the integrity of the hydrogel network. The agglomeration of nanoparticles ATR NPs at higher concentrations like 2–3 wt% resulted in a reduced compressive strength. These data are in agreement with SEM images (Fig. 2A) [70,71].

According to obtained results from mechanical, swelling, and degradation analyses and SEM images, CAO/ATR-1 was selected as a representative of hybrid hydrogels for further mechanical investigations. The cyclic compressive loading-unloading tests were carried out at a strain of 50% without resting time between each cycle to evaluate the toughness and energy dissipation of CAO and CAO/ATR-1. According to Fig. 5A, the hysteresis loop and stress of CAO hydrogel revealed an obvious decrease concerning the original cycle, and it was further decreased with the increase in the number of cycles. This might indicate that the hydrogel network was destroyed during the loading–unloading process and could not be fully and quickly recovered. The SEM image in Fig. S3 also confirmed damages in the morphology of CAO hydrogel after the cyclic test in comparison with the morphology before the cyclic test. On contrary, a distinct hysteresis loop in the first cycle was obtained for the CAO/ATR-1 hydrogel (Fig. 5B), indicating that energy could be dissipated by the rapid distraction of physical interactions in the hydrogel network, including hydrophobic association, ionic coordination, and hydrogen bonds. From the second to fifth cycles, the hysteresis loops nearly overlapped with each other, suggesting that the CAO/ATR-1 hydrogel retained the same network structure in the following cycles and exhibited excellent self-recovery. SEM image of CAO/ATR-1 hydrogel before and after the cyclic test confirmed that the hydrogel network was completely preserved and did not get damaged (Fig. S3). Wei et al. [72] similarly indicated that the NPs inside the hydrogel extend the agar chains back to uniform dispersion after compression and effectively preserve the architecture of the hydrogel. Therefore, the presence of ATR nanoparticles containing TA can maintain the hydrogel microstructure during compression. The different morphologies of CAO and CAO/ATR-1 are the results of unrecovered and collapsed polymer chains. Using the obtained cyclic test the toughness and energy dissipation were quantified and presented in Fig. 5C and D. Compared to CAO, the toughness and energy dissipation of CAO/ATR-1 increased to 1.67 ± 0.19 kJ/m^3 and 0.96 ± 0.15 kJ/m^3 in the first loading-unloading cycle, respectively. In the 5th cycle, this value reached 0.69 ± 0.06 and 0.26 ± 0.01 kJ/m^3, respectively. Also, CAO/ATR-1 hydrogel showed stable behavior after the 2nd cycle. This could be due to the formation of an excellent physical cross-linking network with strong hydrogen bonding between the polymer chains and ATR NPs, and the metal ion interactions between carboxylic acids and Ca^{2+}. Those non-covalent bonds effectively

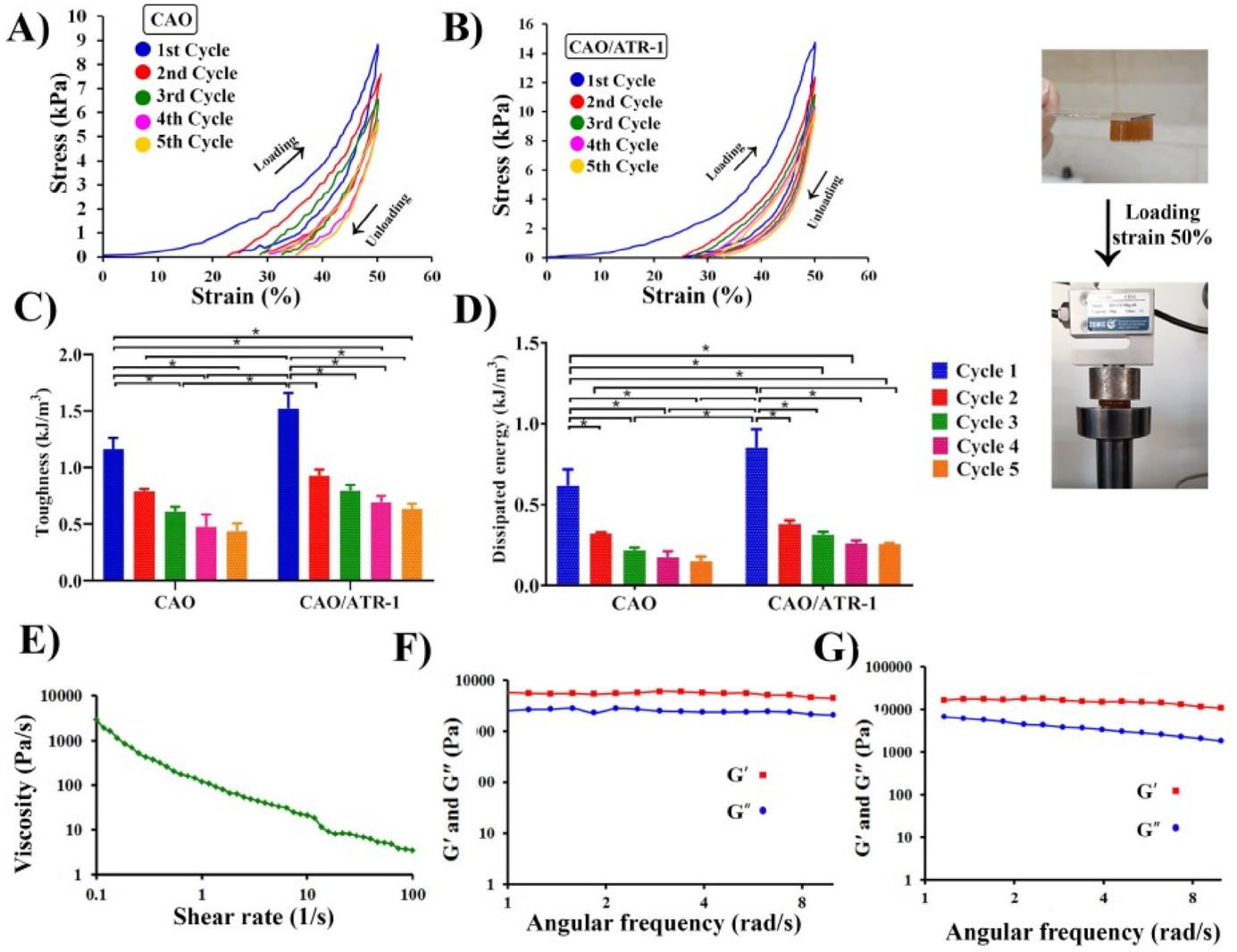

Fig. 5. The cyclic mechanical properties of CAO/ATR hydrogels: The cyclic loading-unloading curves of A) CAO and B) CAO/ATR-1 (at 50% strain). C) Toughness and D) and energy dissipation of CAO and CAO/ATR-1 (*: $p < 0.05$). E) The viscosity change of CAO/ATR-1. Dynamic frequency sweeps of F) CAO, G) CAO/ATR-1.

improved the energy dissipation of the hybrid hydrogel under large strains, so that the CAO/ATR-1 hydrogel dissipated energy more efficiently than the CAO hydrogel under deformation, leading to better toughness with the cooperation of ATR NPs (Fig. 4D). The restoring of a portion of dynamic reversible non-covalent interactions before the next loading might be the reason for this phenomenon. This behavior in the presence of ATR NPs was based on polymer interaction and is in agreement with the literature [67,73].

The mechanical performances of the cross-linked hydrogels were also studied through the dynamic frequency sweep rheological experiments. According to Fig. 5E, increasing the shear rate from 10^{-1} to 10^{2} s^{-1} reduced the viscosity from 10^{3} to 10° Pa s^{-1}. This shear-thinning behavior could be attributed to the shear-induced breaking of the dynamic hydrogel network that enhances the self-healing and injectability of the hydrogels [74]. Also, electrostatic interactions between ATR NPs and polymeric networks enhanced this shear-thinning behavior [75]. Fig. 5F and G show the storage moduli (G′) and loss moduli (G″) of the CAO and CAO/ATR-1 as a function of angular frequency at 37 °C. The G′ value was consistently greater than the G″ value across the entire frequency range, indicating that the hydrogels were mechanically robust and stable, behaving as elastic solids. Also, the G′ value of CAO/ATR-1 was higher than CAO in this frequency range, confirming that the addition of NPs stiffened the hydrogel. In addition, CAO/ATR-1 revealed an enhanced distance between G′ and G″ with the increase of angular frequency, suggesting the nature of the hydrogel dynamic network. In conclusion, the presence of ATR enhanced the mechanical performance of hybrid CAO hydrogels.

3.4. Self-healing ability of CAO/ATR hybrid hydrogel

Hydrogel bioadhesives may bear external mechanical forces after application onto the defect site. The self-healing ability of hydrogels can greatly prolong the lifespan of bioadhesives. The self-healing behavior of CAO/ATR-1 hydrogels was observed in Fig. 6A. After putting the two pieces in contact with each other for 3 h at 25 °C, two semicircular hydrogels (one of which was colored with rhodamine B) were integrated as a whole. The red color was spread to the other side, and the boundaries between the different colored pieces became obscure. Moreover, the healed hydrogel disks did not crack when lifted with the forceps and maintained their shape and integrant after being immersed in PBS (pH = 7.0) for 3 h. The spread of the rhodamine B color throughout the hydrogel indicated that the hydrogel had good self-healing ability. The presence of dynamic covalent bonds in the hydrogel networks, such as Schiff-base reaction and high reversible intermolecular hydrogen bonding, could be the main cause of the rapid self-healing. The self-healing ability of CAO/ATR hydrogels was primarily due to the contribution of reversible chemical covalent bonds (imine bonds) and physical non-covalent interactions (hydrogen bonding, electrostatic interaction, and π-π stacking). The self-healing behaviors are depicted in Fig. 6B. The basis of self-healing hydrogels is quick equilibrium between the reversible separation and recombination of components occurring simultaneously and continuously, whether chemical or physical. This implies that active sites are necessary for the construction of gel networks. The studies indicated that the hydrogels produce local “mobile phases” in or around the injured area in reaction to the damage. This “mobile phase” can lead to joining and filling the injured area to repair the hydrogels [76].

To evaluate the strength of the CAO and CAO/ATR hydrogels after the self-healing test, strain amplitude sweep measurements were performed at 37 °C. Fig. 6C and D shows that G′ and G″ of hydrogels remained almost constant until the strain reached 5% and 10%, respectively. It shows good viscoelastic characteristics of both hydrogels, which resisted structure failure until high strains [77]. It suggested that the CAO/ATR-1 could sustain relatively larger elastic deformation than that of the CAO. So the addition of ATR NPs provided a further stronger gel. However, when the strain was further increased, the storage modulus curve intersected with the loss modulus curve at about 78% for CAO and 120% for CAO/ATR-1, indicating the critical point, which stated the hydrogel was

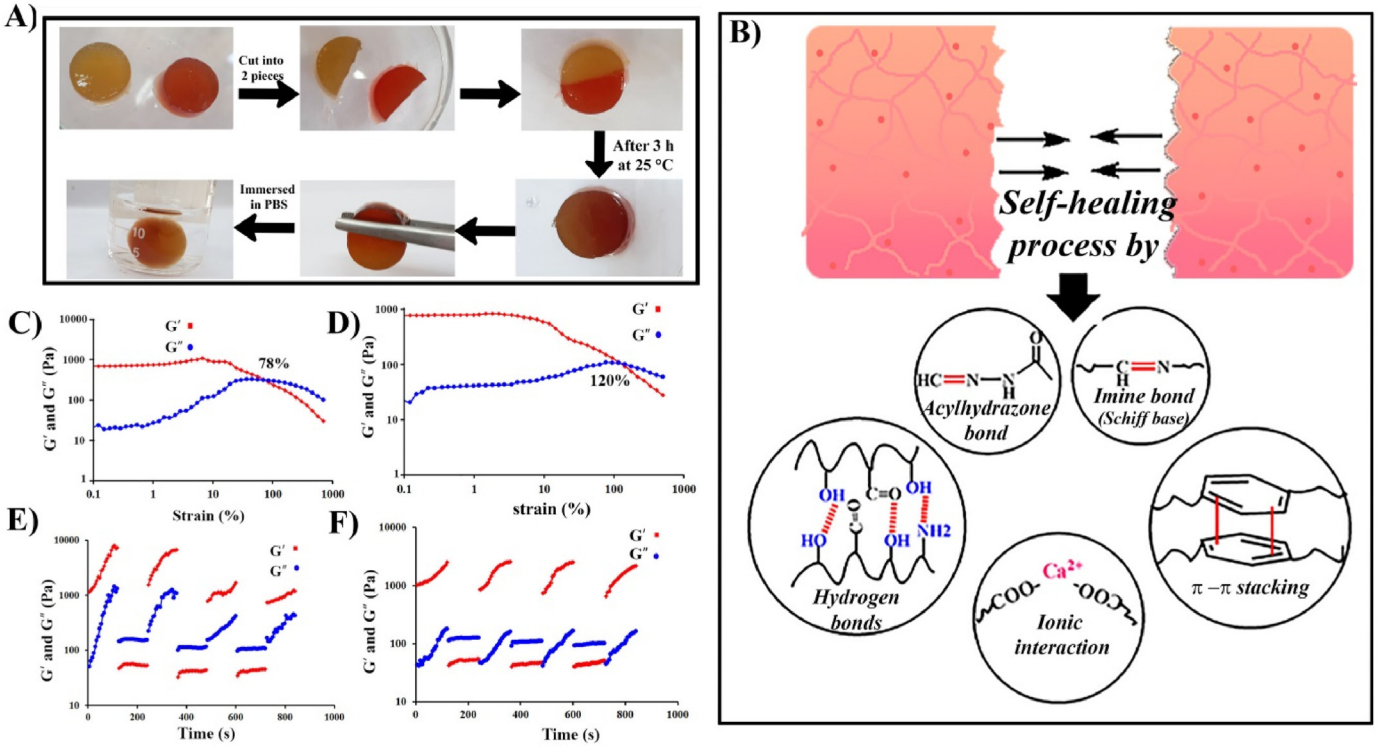

Fig. 6. Self-healing properties of CAO/ATR hybrid hydrogels: A) Images showing the macroscopic self-healing behavior. B) The schematic representation of self-healing mechanisms. The strain amplitude sweep test (10–800%) for C) CAO and D) CAO/ATR-1 at a fixed angular frequency (1 rad s^{-1}). Alternate step strain sweep test for E) CAO and F) CAO/ATR-1 with small strain (1.0%) to subsequent large strain (300%) with 120 s for every strain interval.

between solid and fluid. It stated that when the critical strain of the hydrogel network is exceeded, it could be broken, turning into a fluid-like [78]. Thereafter, the possibility of recovery in the hydrogel structure was evaluated using the continuous cyclic strain test (1% strain → 300% strain → 1% strain) at a constant angular frequency (10 rad s^{-1}). According to Fig. 6E and F, at a 300% strain exceeding the critical strain, the hydrogels were converted to a sol state ($G' < G''$). Once the strain returned to 1%, the gel reformed again, and the G' and G'' values immediately recovered to the initial values without any loss. In addition, the loss factor, defined as the ratio between the loss and storage modulus ($\tan \delta = G''/G'$), was similarly measured. For CAO hydrogel after every severe strain, tan δ decreased slightly, while CAO/ATR-1 revealed the fast self-recovery of the network after the removal of high strain, which was in accordance with cyclic testing. This is also confirmed by the full recovery of G' for CAO/ATR-1 at a low strain of 1%. On the other hand, G' of CAO hydrogel decreased in value, implying that the hydrogel did not completely recover. The collapse and recovery behaviors of the hydrogel network could be alternately repeated several times, demonstrating the rapid and highly efficient self-healing capacity of the hydrogel. Additionally, the hybrid hydrogel due to possessing the physical crosslinking and reversible Schiff-base network showed a shear-thinning property (Fig. 5E), which was helpful for injecting the hydrogels.

3.5. Adhesive properties and injectability of CAO/ATR hybrid hydrogel

According to Fig. 7A, CAO/ATR-1 hydrogel could attach to a patch of moist cow skin and distort without coming off or breaking, and also could be completely peeled off from the skin's surface without causing tissue damage. The lap-shear test was used to assess the adhesive strength of hydrogels. Results are presented in Fig. 7B. It was found that the addition of ATR NPs in the CAO hydrogel network significantly increased the adhesive strength from 8 ± 3 kPa to 28 ± 5 kPa ($P < 0.05$). It might be due to the presence of free hydroxyl groups in TA, which were not integrated with the CAO chains. TA has catechol in its structure, which could increase the material's adhesiveness. The hydroxyl and amine groups of the hybrid hydrogel may bind to phospholipid molecules on cell membranes through electrostatic and hydrophobic interactions, offering a hypothetical mechanism for tissue adherence of these hydrogels. Additionally, the cation-π interaction and π-π stacking between phenol in the hydrogel matrix, caused by phenol moieties conjugated to the ATR NPs, and tyrosine on the tissue, resulted in the adhesive property of CAO/ATR-1. On the other hand, the remaining aldehyde groups in the CAO hydrogels could be employed to interact with the amino groups of lysine and hydroxylysine in tissues, which would improve the hydrogels' adhesive strength. To better evaluate the experimental hydrogels, known values for commercial medical adhesives, such as fibrin glue and cyanoacrylate, are used here as examples. Fibrin glue has low adhesive strength (<15 kPa) and high conformity to tissues, and cyanoacrylate (13.7 MPa), with high adhesive strength, forms a rigid and inflexible bond to tissues, which due to its high cell and tissue toxicity has limited application in wound treatment [79,80]. The lap shear adhesion strength of CAO/ATR-1 hybrid hydrogel was also compared with other hydrogel dressings (normally 5.5–21 kPa) (Fig. 7C) [80,81]. It could be found that hydrogels containing carboxylated chitosan or oxidized alginate revealed lower adhesion strength compared to the CAO/ATR-1 hybrid hydrogel.

An ideal adhesive hydrogel for wound dressings should also be injected directly using a syringe and create gels *in situ* at wound sites. Fig. 7D depicts the injectability of the CAO/ATR-1 hydrogel. CAO/ATR-1 could be easily extruded through a syringe without clogging and extruded with the characters "IUT". The dynamic nature and shear-

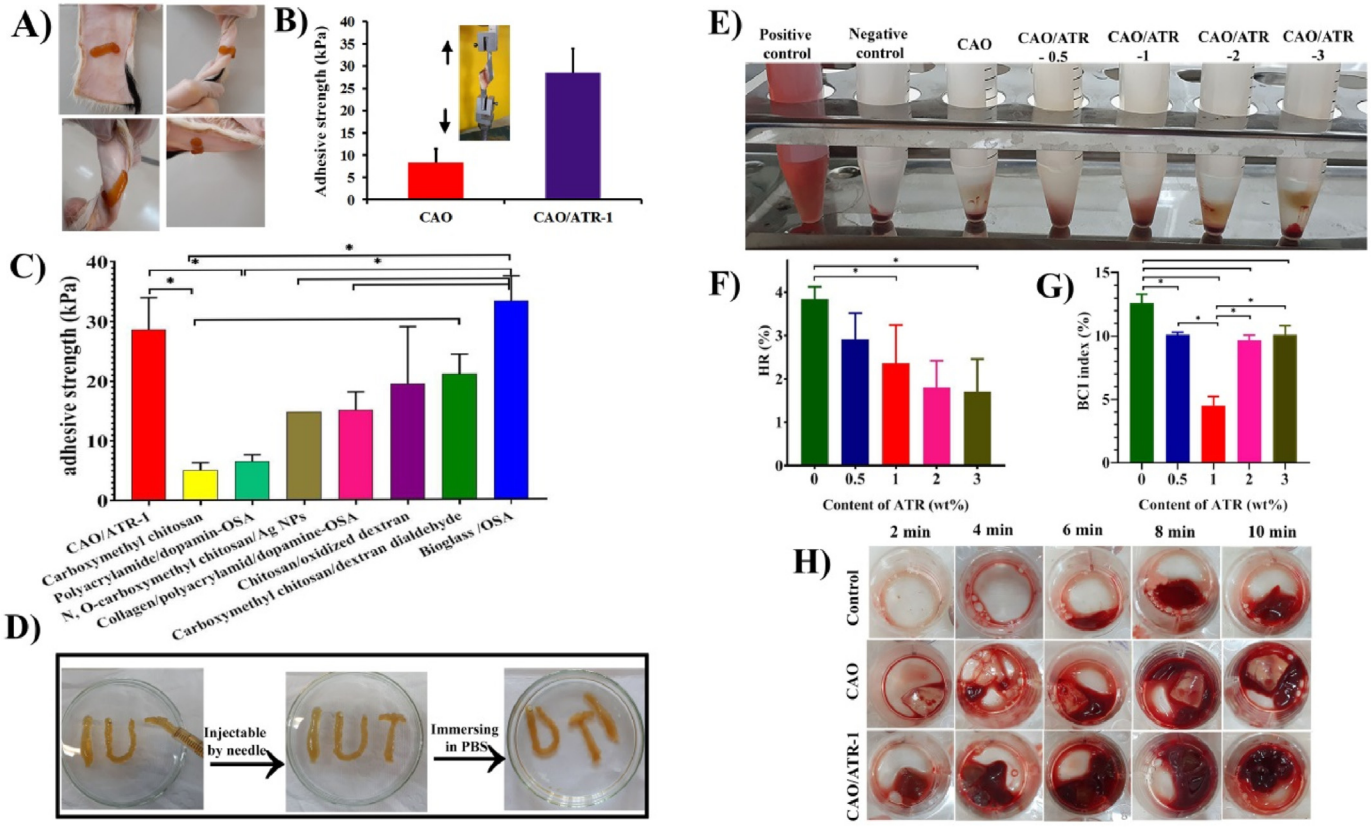

Fig. 7. A) Photos of CAO/ATR-1 adhered to cow skin under different deformations, B) Quantified adhesive strength of CAO/ATR-1 compared to CAO. C) Comparison of the adhesive strength of CAO/ATR-1 hybrid hydrogel with previous studies [82–87]. D) Injection of a CAO/ATR-1 and immersion into PBS. E) Photograph images of *in vitro* hemolysis test, F) HR% of RBCs contacting with the hydrogels (n = 3), G) BCI index of hydrogels (*: $p < 0.05$). H) The photograph images of clotting time during 10 min.

thinning property of CAO/ATR-1 hydrogel supported its extrusion. In addition, the hydrogel kept its integrity after immersion in PBS (pH = 7.0), indicating that the CAO/ATR-1 hydrogel had good shape fidelity.

3.6. Blood-CAO/ATR hybrid hydrogel interaction

The hemolytic activity test was used to assess the hemocompatibility of hybrid hydrogels. Fig. 7E shows an obvious color difference between the hydrogel-treated groups and the positive control group. The hydrogel-treated groups presented a nearly clear solution with a canary yellow color, which is similar to that of normal saline solution (a negative control) since the undamaged red blood cells (RBCs) settled down to the bottom of the tube. However, the positive control group (deionized water) was bright red and indicated that hemoglobin (Hb) leaked into the solution. In comparison to the positive control with a hemolysis ratio of 100%, quantitative evaluation of all hydrogels revealed a low hemolysis ratio (4%) (Fig. 7F). For example, CAO and CAO/ATR-1 had hemolysis ratios of 4.1 ± 0.1% and 2.3 ± 0.1%, respectively. Our results revealed that the hemolysis ratios of CAO/ATR hydrogels were less than the international standard of 5%, indicating that they have excellent hemocompatibility suitable for various wound dressing applications [26]. Hemolysis is the loss of membrane integrity of RBCs, leading to the leakage of Hb into the blood plasma. Adhesive hydrogels might affect the membrane integrity of RBCs through mechanical damage or reactive oxygen species [88]. In addition, the hemolytic property of hydrogels can also be influenced by their shape, surface charge, and chemical composition [89]. As a hemostatic mechanism, when a hydrogel comes into contact with blood, hydrogel interacts with blood plasma proteins, resulting in rapid blood protein barrier membrane formation within a few seconds via ionic/covalent/hydrogen bonds and reversible hydrophobic interactions. Through this process, the hydrogel formed robust physical membranes at the bleeding site, leading to successful hemostasis regardless of blood status.

A blood clotting index (BCI) is normally used to describe the degree of blood-hemostasis clot formation. Higher blood clotting ability caused higher stability of the clot and lowered flowing behavior, which led to a decrease in the BCI%. So, low BCI values indicated high blood clotting activity [60]. By increasing the ATR NPs concentration from 0 wt% to 0.5 wt%, and 1 wt%, the BCI% of the CAO/ATR hybrid hydrogels was decreased 3-fold from 12.6 ± 0.3% to 10.1 ± 0.2% and 4.5 ± 0.3% ($p < 0.05$), and then with an increase of ATR NPs content from 2 wt% to 3 wt %, the BCI% value increased from 6.6 ± 0.2% to 7.5 ± 0.5% ($p < 0.05$) (Fig. 7G). It might be due to the intense negative charge of TA in the ATR NPs structure and the porous structure of hybrid hydrogels. Cheng et al. [90] also demonstrated that the cellulose hybrid containing chitosan with porous structures and better absorbability had better coagulation performance than the cellulose hybrid.

Fig. 7H shows the representative images of coagulated blood in the wells with or without the hydrogels. No obvious blood clot was observed in the control group at the 4 min time point, whereas a small amount of blood clot was observed in the polystyrene well plate after 6 min. By contrast, an obvious clot was visibly observed in the wells containing CAO and CAO/ATR-1 hydrogels. Moreover, the amount of clot gradually increased with increasing blood-sample contacting time, especially for CAO/ATR-1. For instance, the blood clotting time was <4 min for the CAO/ATR-1 hybrid hydrogel, which was shorter than the times for CAO (4 min) and blood alone (6 min). Similar results were reported by Suneetha et al. [91], where after the addition of polydopamine to sodium alginate-polyacrylamide, a reduced blood clotting time was reported. Hydrogels can expedite the clotting process, and CAO/ATR-1 hydrogel has the best effect in promoting coagulation. The hemostatic property of the CAO/ATR hydrogels was likely due to their great water absorption capacity and the electrostatic attraction between the hydrogel and blood. Moreover, hydrogels accelerated blood clotting owing to their abundant positively charged amino groups and calcium ions. The positive charge of hydrogels attracted plasma fibronectins, platelets, and RBCs through electrostatic attraction and facilitated the formation of a substantial amount of fibrin. On the other hand, due to the interactions between blood and the phenolic hydroxyl groups of TA, the ATR NPs containing TA increased blood clotting. The negatively charged polyphenol served as a contact activator, allowing phenolic compounds to activate clotting factors in the body, improving their hemostatic properties [92]. Lamei et al. [93] similarly found that adding TA to a chitosan/poly(vinyl alcohol) nanofibrous scaffold improved hemostatic performance by increasing liquid absorbability and speeding up the aggregation of coagulation components and platelets. Kong et al. [37] also demonstrated that the hemostatic ability of CEC/OSA/CuS hydrogels is attributed to the hemostatic property of chitosan, which could attach to the hemorrhage site and quickly form a blood clotting barrier.

3.7. Antibacterial properties of CAO/ATR hybrid hydrogel

The antibacterial properties of CAO and CAO/ATR-1 hydrogels, and non-cross-linked solutions of OSA/ATR and OSA/anthocyanin, were evaluated against *E. coli* and *S. aureus* by using the disk diffusion method (Fig. 8A and B). The inhibition zone diameters were measured after 24 h. According to Fig. 8A, all samples exhibited antibacterial effects on the two bacteria lines, except CAO, which had no antibacterial activity against *E. coli*. There was no bacteriostatic zone on *E. coli* around the CAO. According to Fig. 8B, the inhibition zone diameter of CAO/ATR-1, OSA/anthocyanine, and OSA/ATR against *E. coli* was estimated at 13 mm, 14 mm, and 16 mm, respectively. It seems that Gram-negative bacteria (*E. coli*) might be more sensitive to the presence of ATR compounds. In the case of *S. aureus*, CAO, CAO/ATR-1, OSA/anthocyanin, and OSA/ATR indicated an inhibition zone with a diameter of 12 mm, 15 mm, 21 mm, and 22 mm, respectively. The presence of a blurry and colored circle in the inhibition zone of OSA/anthocyanin could be attributed to the anthocyanin released from the OSA. It is worth noting that higher antimicrobial activity was observed against *S. aureus* than against *E. Coli* for all samples. These results are in good agreement with the previous report of Grkovic et al. [94] and Zhang et al. [95], who also observed a higher inhibitory effect against Gram-positive bacteria than

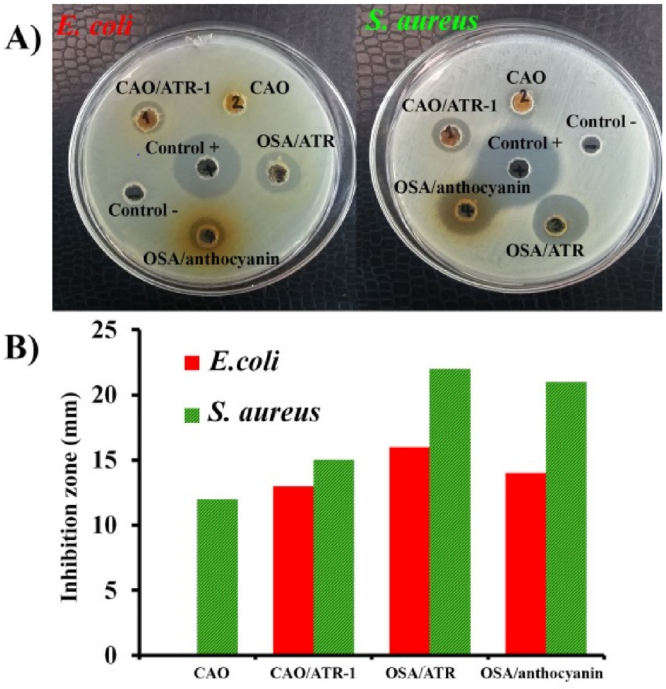

Fig. 8. Antibacterial properties of CAO/ATR hybrid hydrogels: A) Qualitative images of the antibacterial properties and B) amount of inhibition zone of samples against *S. aureus* and *E. coli* bacteria.

Gram-negative bacteria. This behavior might be related to the structure of the bacterial cell envelope. Gram-positive bacteria have an inner membrane and a cell wall, whereas Gram-negative bacteria have an additional outer membrane in the cell envelope [96]. Moreover, the combination of antibacterial properties of chitosan and TA are responsible for the inherent antibacterial capability in TA-reinforced hydrogels. It was assumed that the positively charged surface of amino groups of CEC and the flavylium cation backbone of anthocyanin destabilize the structure of the cell wall of bacteria, causing inhibition of normal bacterial metabolism [94]. Therefore, protonated amino groups can kill bacteria on the surfaces of the hydrogels by electrostatic interactions between the protonated amino groups and the phosphoryl groups of the phospholipid components of cell membranes. However, the precise antibacterial mechanisms of TA are controversial. The cytoplasmic membrane's instability, the decreased enzyme activity by interacting with bacterial proteins, or the membrane's increased permeability are only a few of the possible mechanisms that could contribute to TA's antibacterial properties [97]. Also, the presence of carboxylic acid groups in the structure of the hybrid hydrogel could act as bacteriostatic and prevent the growth of bacteria. In comparison with OSA/ATR and OSA/anthocyanin solutions, the slight decrease in antibacterial properties of CAO/ATR-1 hybrid hydrogel might be due to the embedding of ATR NPs among 3D polymer chains of CAO which led to the slow release of Ag ions. Our results suggested that the antibacterial properties of CAO/ATR-1 hydrogel were considerably greater than those of unmodified CAO for both Gram-positive and Gram-negative bacteria.

3.8. Cell-CAO/ATR hybrid hydrogel interaction

Bioadhesive hydrogels should possess good cytocompatibility when used as a hemostatic agent and wound dressing. *In vitro* cell viability experiment was performed to evaluate the biocompatibility of CAO and CAO/ATR-1 using a L929 fibroblast cell line (Fig. 9). Fig. 9A shows live/dead staining images of the fibroblasts after being cultivated on hydrogels for 1 and 5 days. These images demonstrated that the number of live (green) cells was much higher than the number of dead (red) cells, and also, the number of green cells increased in both CAO and CAO/ATR-1 after 5 days of incubation. It showed that the synthesized hydrogels did not adversely affect cell viability. The quantitative analysis revealed that the viability of fibroblasts cultured on CAO/ATR-1 hybrid hydrogel was 98.3% ± 0.9% and 98.9% ± 0.6% after 1 and 5 days of culture, respectively, which was significantly higher than that of CAO (94.7% ±

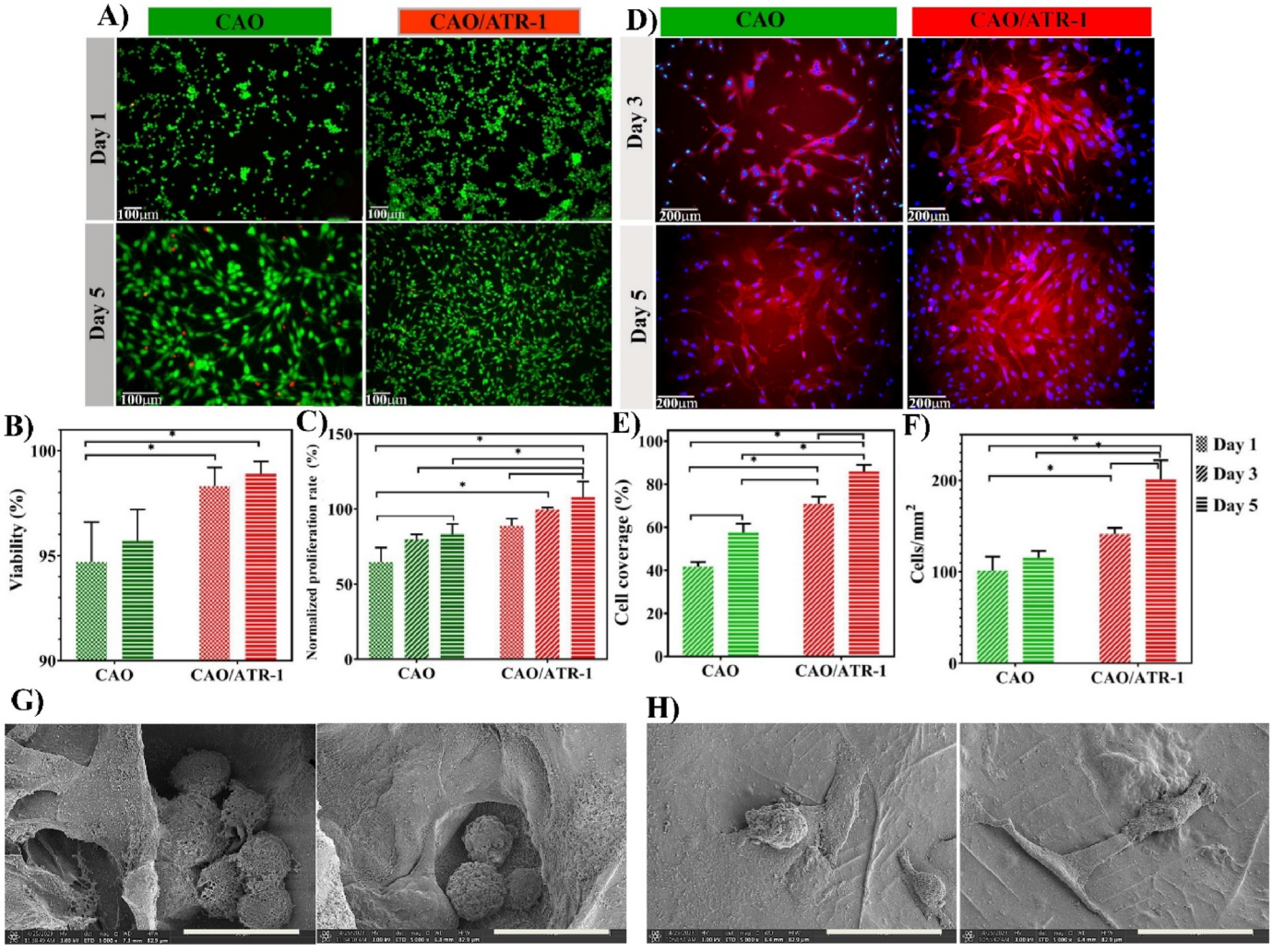

Fig. 9. Cell compatibility of CAO/ATR hybrid hydrogels: A) Fluorescence images of live/dead assay of fibroblasts seeded on the CAO and CAO/ATR-1 at days 1 and 5 of culture. B) Quantified cell viability results obtained from live/dead assay. C) The normalized proliferation rate of fibroblasts cultured on CAO and CAO/ATR-1 using MTT assay. The absorbance was normalized against the control (TCP) at each time interval. D) Fluorescence images of the actin cytoskeleton of the fibroblasts after 3 and 5 days of culture on hydrogels. E) Cell coverage, the fraction of area covered with cell clusters after 3 and 5 days. F) The cell density was calculated based on stained nuclei on days 3 and 5 (*: $p < 0.05$). The SEM images of cells cultured on G) CAO and H) CAO/ATR-1 for 3 days, respectively. The scale bars in all the images represent 30 μm.

1.9% and 95.6% ± 1.5% after 1 and 5 days, respectively) (Fig. 9B). From Fig. 9A, it could be found that a higher number of cells has covered the surface of the hydrogel CAO/ATR-1 than the CAO after 5 days of culture. This phenomenon could be related to the numerous active sites and high affinity of ATR NPs, as well as the porous structure of the hydrogels, which could encourage cell adhesion and proliferation. The proliferation rate of the cells in contact with the hydrogels was measured using an MTT assay, and this assay further confirmed the cytocompatibility of the materials (CAO and CAO/ATR-1 hydrogels) (Fig. 9C). The results showed that the normalized proliferation rate on CAO/ATR-1 was greater than the CAO hydrogel during the culture period. According to Fig. 9C, the normalized proliferation rate of cells cultured with the CAO/ATR-1 hydrogel enhanced from 88.6 ± 4.9% to 107.8 ± 10.3% with increasing culture time from 1 day to 5 days, while the normalized proliferation rate in contact with CAO was 64.7 ± 9.5%, and 83.2 ± 6.8% after 1, and 5 days of culture, respectively.

To visualize the fibroblast cytoskeleton, F-actin/nuclei staining was performed (Fig. 9D). The nuclei and actin cytoskeleton of fibroblast were stained with DAPI (blue) and rhodamine-phalloidin (red), respectively. F-actin filaments were uniformly and densely distributed and spread over the CAO and CAO/ATR-1 hydrogels. However, cell spreading was more substantial on CAO/ATR-1. In other words, the hydrogels containing ATR NPs were more effective at developing a connection between hybrid hydrogel networks and fibroblast cells. In order to determine the effect of substrate on cell spreading, cell coverage on various hydrogels was measured (Fig. 9E). The hydrogel of CAO/ATR-1 showed a higher cell coverage (~71% and 86%, respectively) compared to CAO on day 3 and day 5, which were 42% and 57%, respectively. Additionally, the cell density was calculated after 3 and 5 days of culture by counting stained nuclei (Fig. 9F). We observed that the number of cells on the sample's surfaces increased from day 3 to day 5 as a result of cell adaptation to their environment over time. For instance, the density of cells on the CAO hydrogel increased from 101 ± 15 cells.mm^{-2} to 115 ± 7 cells.mm^{-2}, and on the CAO/ATR-1 from 141 ± 7 cells.mm^{-2} to 200 ± 21 cells.mm^{-2}, after days 3 and 5 of culture, respectively. Moreover, the morphology of the fibroblasts on the hydrogel surfaces was investigated using SEM (Fig. 9G and **H)**. The cells were well spread and adhered to the surface of the hydrogels. In Fig. 9G, it can be seen that the cells could even immigrate to the pores and spread their filopodia on the surface of the hydrogels. It must be noted that the growth and spread of cells on the surface of CAO containing ATR NPs (CAO/ART-1) were remarkably better than that of the CAO sample after 3 days of culture. It could be due to the increased hydrophilicity and the presence of biological signals originating from CAO/ATR-1. Hence, it seems that the hydrogel with 1% ATR NPs provides a better environment for fibroblast cell adhesion, which is in agreement with other biological studies presented in this work.

Our results revealed that, during 5 days of culture, ATR nanoparticles did not cause any cytotoxicity, and the viability and proliferation of fibroblasts were maintained. These observations are in agreement with Lopez-Carrizales et al. [98], where they reported the viability of more than 95% of fibroblast in contact with chitosan loaded with a low concentration of Ag NPs. Khamira et al. [99] similarly showed that the bacterial cellulose films containing Ag NPs are highly efficient in wound healing as Ag NPs could stimulate the migration and the proliferation of the cells. They reported that Ag NPs increased the differentiation of fibroblasts to myofibroblasts and increased wound healing via secreting elastin and actin filaments. However, previous studies revealed that the proliferation rate of cells in contact with a high concentration of Ag NPs loaded constructs was slower, owing to the acute toxic effect of Ag NPs on various mammalian cells [100,101]. Furthermore, Hernandez-Rangel et al. [102] studied the biocompatibility of chitosan hydrogels with different concentrations of AgNPs on fibroblast cells for 8 days. They found out that Ag NPs revealed dose-dependent cytotoxicity and concluded that high concentrations of AgNPs affected the spreading of the fibroblasts and their adhesion ability. In addition, other studies suggested that the toxicity mechanism of AgNPs on eukaryotic cells is a decrease in the reduction function of mitochondria, higher generation of reactive oxygen species (ROS), and higher DNA damage [103,104]. According to our results, the incorporation of 1 wt% ATR NPs in the hydrogel matrix was sufficient to destruct bacterial cells without inducing any cytotoxicity of fibroblasts. In this regard, surface modification of AgNPs with TA and RC could reduce the usual agglomeration issue of the particles and support the homogenous dispersion of them in the matrix which improves the cell interaction. Furthermore, the higher proliferation of cells in contact with CAO/ATR-1 hydrogel might be due to the catechol groups of TA forming strong connections with fibroblasts through interactions with imidazoles or thiols on the cell membrane of fibroblasts. A similar result was reported for other hydrogels such as TA cross-linked poly(vinyl alcohol)/carboxymethyl chitosan [105] and polyvinyl alcohol/collagen/TA [106] in contact with natural human dermal fibroblasts. The presence of TA as a cross-linker can significantly stimulate fibroblast growth and proliferation. It has been shown in the literature that TA suppressing TGF-β1 can lead to proliferating, migrating, and expressing certain genes necessary for ECM remodeling in fibroblasts. In addition, the presence of anthocyanins doesn't have any negative effect on cell behavior [107]. Therefore, we investigated *in vitro* cell and materials interactions and showed that the CAO/ATR-1 hydrogel is highly cytocompatible and noncytotoxic in comparison with the CAO and can be potentially used in wound healing applications.

Finally, CAO/ATR hybrid hydrogels with significantly essential features such as maintaining wound moisture, suitable mechanical properties, self-healing, low cost, and easy processing, adhesiveness, colorimetric measurement of pH as an indicator of bacterial infection, and intrinsic antibacterial properties can be a promising dressing in wound healing.

4. Conclusion

This study successfully developed an injectable multifunctional wound dressing hydrogel through the reversible Schiff-base bonds between amino groups on CEC or ADH and aldehyde groups on OSA and ionic cross-linking between Ca^{2+} ions and carboxyl groups of OSA. In this process, ATR NPs were used as a pH-responsive indicator and an antibacterial agent. The CAO/ATR-1 hybrid hydrogel demonstrated higher adhesive properties (28 kPa) than that of the CAO hydrogel (8 kPa). In addition, the CAO/ATR hydrogel was sensitive to pH variations and exhibited a color change from red to green, along with pH variations ranging from 3.0 to 9.0. The hybrid hydrogels exhibited outstanding hemostatic ability and a decreased *in vitro* blood clotting time due to their porous structure and the hemostatic effect of CEC and TA. The hybrid hydrogel had a good antibacterial impact on the growth rate of *E. coli* and *S. aureus* after ATR NP loading. An *in vitro* cytotoxicity experiment confirmed that the CAO/ATR hydrogels had better cytocompatibility with fibroblasts and maintained their vitality and proliferation. In summary, CAO/ATR hydrogel has the potential to be used as an excellent wound-dressing hydrogel for promoting wound healing and pH monitoring at the same time.

Author contributions

Elham Khadem: Conceptualization, Methodology, Validation, Formal analysis, Investigation, Data curation, Writing – original draft, Writing – review & editing, Visualization. **Mahshid Kharaziha**: Supervision, Conceptualization, Methodology, Validation, Writing – review & editing, Visualization. **Sahar Salehi**: Supervision, Funding acquisition, Conceptualization, Methodology, Validation, Writing – review & editing.

Declaration of competing interest

The authors declare that they have no known competing financial interests or personal relationships that could have appeared to influence

the work reported in this paper.

Data availability

Data will be made available on request.

Acknowledgments

This work was supported by Deutsche Forschungsgemeinschaft DFG (SA 3575/2–1) Project number 497840077, SA 3575/1-1 and SFB/TRR225 (Project number 326998133 – subproject B03-PI Sahar Salehi). Furthermore, the Research Affairs Division of the Isfahan University of Technology (IUT), the National Elite Foundation (NEF), and Iran National Science Foundation (INSF), (99003685 Grant Number) financially supported this research. Authors gratefully acknowledge the support of the Alexander von Humboldt (AvH) Foundation for the experience researcher fellowship to Mahshid Kharaziha. We would like to acknowledge the guidance and help of Mr. Hamidreza Mokhtari. We thank Elise Linsdorf for the proofreading.

Appendix A. Supplementary data

Supplementary data to this article can be found online at https://doi.org/10.1016/j.mtbio.2023.100650.

References

[1] S. Pourshahrestani, E. Zeimaran, N.A. Kadri, N. Mutlu, A.R. Boccaccini, Polymeric hydrogel systems as emerging biomaterial platforms to enable hemostasis and wound healing, Advanced Healthcare Materials 9 (20) (2020), 2000905.
[2] S. Ahadian, R.B. Sadeghian, S. Salehi, S. Ostrovidov, H. Bae, M. Ramalingam, A. Khademhosseini, Bioconjugated hydrogels for tissue engineering and regenerative medicine, Bioconjugate Chem. 26 (10) (2015) 1984–2001.
[3] N. Rajabi, M. Kharaziha, R. Emadi, A. Zarrabi, H. Mokhtari, S. Salehi, An adhesive and injectable nanocomposite hydrogel of thiolated gelatin/gelatin methacrylate/Laponite® as a potential surgical sealant, J. Colloid Interface Sci. 564 (2020) 155–169.
[4] I. Apsite, S. Salehi, L. Ionov, Materials for smart soft actuator systems, Chem. Rev. 122 (1) (2021) 1349–1415.
[5] M. Rodrigues, N. Kosaric, C.A. Bonham, G.C. Gurtner, Wound healing: a cellular perspective, Physiol. Rev. 99 (1) (2019) 665–706.
[6] A.C.d.O. Gonzalez, T.F. Costa, Z.d.A. Andrade, A.R.A.P. Medrado, Wound healing-A literature review, An. Bras. Dermatol. 91 (2016) 614–620.
[7] T. Guinovart, G. Valdés-Ramírez, J.R. Windmiller, F.J. Andrade, J. Wang, Bandage-based wearable potentiometric sensor for monitoring wound pH, Electroanalysis 26 (6) (2014) 1345–1353.
[8] S. Schreml, R.M. Szeimies, S. Karrer, J. Heinlin, M. Landthaler, P. Babilas, The impact of the pH value on skin integrity and cutaneous wound healing, J. Eur. Acad. Dermatol. Venereol. 24 (4) (2010) 373–378.
[9] A. Tamayol, M. Akbari, Y. Zilberman, M. Comotto, E. Lesha, L. Serex, S. Bagherifard, Y. Chen, G. Fu, S.K. Ameri, Flexible pH-sensing hydrogel fibers for epidermal applications, Advanced healthcare materials 5 (6) (2016) 711–719.
[10] M. Qin, H. Guo, Z. Dai, X. Yan, X. Ning, Advances in flexible and wearable pH sensors for wound healing monitoring, J. Semiconduct. 40 (11) (2019), 111607.
[11] T.R. Dargaville, B.L. Farrugia, J.A. Broadbent, S. Pace, Z. Upton, N.H. Voelcker, Sensors and imaging for wound healing: a review, Biosens. Bioelectron. 41 (2013) 30–42.
[12] E. Khadem, M. Kharaziha, H.R. Bakhsheshi-Rad, O. Das, F. Berto, Cutting-edge progress in stimuli-responsive bioadhesives: from synthesis to clinical applications, Polymers 14 (9) (2022) 1709.
[13] Q. Ma, Y. Ren, Z. Gu, L. Wang, Developing an intelligent film containing Vitis amurensis husk extracts: the effects of pH value of the film-forming solution, J. Clean. Prod. 166 (2017) 851–859.
[14] E. Gianino, C. Miller, J. Gilmore, Smart wound dressings for diabetic chronic wounds, Bioengineering 5 (3) (2018) 51.
[15] M.A. Mohamed, A. Fallahi, A.M. El-Sokkary, S. Salehi, M.A. Akl, A. Jafari, A. Tamayol, H. Fenniri, A. Khademhosseini, S.T. Andreadis, C. Cheng, Stimuli-responsive hydrogels for manipulation of cell microenvironment: from chemistry to biofabrication technology, Prog. Polym. Sci. 98 (2019), 101147.
[16] P. Mostafalu, A. Tamayol, R. Rahimi, M. Ochoa, A. Khalilpour, G. Kiaee, I.K. Yazdi, S. Bagherifard, M.R. Dokmeci, B. Ziaie, Smart bandage for monitoring and treatment of chronic wounds, Small 14 (33) (2018), 1703509.
[17] H. Derakhshandeh, S.S. Kashaf, F. Aghabaglou, I.O. Ghanavati, A. Tamayol, Smart bandages: the future of wound care, Trends Biotechnol. 36 (12) (2018) 1259–1274.
[18] M. Mir, M.N. Ali, A. Barakullah, A. Gulzar, M. Arshad, S. Fatima, M. Asad, Synthetic polymeric biomaterials for wound healing: a review, Progress in biomaterials 7 (1) (2018) 1–21.
[19] N. Asadi, H. Pazoki-Toroudi, A.R. Del Bakhshayesh, A. Akbarzadeh, S. Davaran, N. Annabi, Multifunctional hydrogels for wound healing: special focus on biomacromolecular based hydrogels, Int. J. Biol. Macromol. 170 (2021) 728–750.
[20] S. Mallakpour, E. Khadem, Construction of crosslinked chitosan/nitrogen-doped graphene quantum dot nanocomposite for hydroxyapatite biomimetic mineralization, Int. J. Biol. Macromol. 120 (2018) 1451–1460.
[21] Z. Aslani, N. Nazemi, N. Rajabi, M. Kharaziha, H. Bakhsheshi-Rad, M. Kasiri-Asgarani, A. Najafinezhad, A. Ismail, S. Sharif, F. Berto, Antibacterial activity and cell responses of vancomycin-loaded alginate coating on ZSM-5 scaffold for bone tissue engineering applications, Materials 15 (14) (2022) 4786.
[22] A. Golshirazi, N. Golafshan, M. Kharaziha, Multilayer self-assembled kappa carrageenan/chitosan: heparin coating on Mg alloys for improving blood compatibility, Mater. Today Commun. 32 (2022), 104085.
[23] J. Huang, H. Xie, H. Ye, T. Xie, Y. Lin, J. Gong, C. Jiang, Y. Wu, S. Liu, Y. Cui, Effect of carboxymethylation degree on the adsorption capacity of Cu (II) by N-(2-carboxyethyl) chitosan from squid pens, Carbohydr. Polym. 138 (2016) 301–308.
[24] L. Wang, L. Sun, Z. Gu, W. Li, L. Guo, S. Ma, L. Guo, W. Zhang, B. Han, J. Chang, N-carboxymethyl chitosan/sodium alginate composite hydrogel loading plasmid DNA as a promising gene activated matrix for in-situ burn wound treatment, Bioact. Mater. 15 (2022) 330–342.
[25] S. Reakasame, A.R. Boccaccini, Oxidized alginate-based hydrogels for tissue engineering applications: a review, Biomacromolecules 19 (1) (2018) 3–21.
[26] N. Golafshan, R. Rezahasani, M.T. Esfahani, M. Kharaziha, S. Khorasani, Nanohybrid hydrogels of laponite: PVA-Alginate as a potential wound healing material, Carbohydr. Polym. 176 (2017) 392–401.
[27] U.S. Malik, M.B.K. Niazi, Z. Jahan, M.I. Zafar, D.-V.N. Vo, F. Sher, Nano-structured dynamic Schiff base cues as robust self-healing polymers for biomedical and tissue engineering applications: a review, Environ. Chem. Lett. (2021) 1–23.
[28] Z. Wei, J.H. Yang, Z.Q. Liu, F. Xu, J.X. Zhou, M. Zrínyi, Y. Osada, Y.M. Chen, Novel biocompatible polysaccharide-based self-healing hydrogel, Adv. Funct. Mater. 25 (9) (2015) 1352–1359.
[29] J. Cao, L. Xiao, X. Shi, Injectable drug-loaded polysaccharide hybrid hydrogels for hemostasis, RSC Adv. 9 (63) (2019) 36858–36866.
[30] Z. Wei, J. Zhao, Y.M. Chen, P. Zhang, Q. Zhang, Self-healing polysaccharide-based hydrogels as injectable carriers for neural stem cells, Sci. Rep. 6 (1) (2016) 1–12.
[31] Z. Güngör, Hava Ozay, Ultra-fast pH determination with a new colorimetric pH-sensing hydrogel for biomedical and environmental applications, React. Funct. Polym. 180 (2022), 105398.
[32] F. Paladini, M. Pollini, Antimicrobial silver nanoparticles for wound healing application: progress and future trends, Materials 12 (16) (2019) 2540.
[33] S. Pang, Y. Gao, F. Wang, Y. Wang, M. Cao, W. Zhang, Y. Liang, M. Song, G. Jiang, Toxicity of silver nanoparticles on wound healing: a case study of zebrafish fin regeneration model, Sci. Total Environ. 717 (2020), 137178.
[34] J. Chen, S. Dai, L. Liu, M.F. Maitz, Y. Liao, J. Cui, A. Zhao, P. Yang, N. Huang, Y. Wang, Photo-functionalized TiO2 nanotubes decorated with multifunctional Ag nanoparticles for enhanced vascular biocompatibility, Bioact. Mater. 6 (1) (2021) 45–54.
[35] E. Khadem, M. Kharaziha, Red cabbage anthocyanin-functionalized tannic acid-silver nanoparticles with pH sensitivity and antibacterial properties, Mater. Chem. Phys. (2022), 126689.
[36] P. Orlowski, M. Zmigrodzka, E. Tomaszewska, K. Ranoszek-Soliwoda, M. Czupryn, M. Antos-Bielska, J. Szemraj, G. Celichowski, J. Grobelny, M. Krzyzowska, Tannic acid-modified silver nanoparticles for wound healing: the importance of size, Int. J. Nanomed. 13 (2018) 991.
[37] Y. Kong, Z. Hou, L. Zhou, P. Zhang, Y. Ouyang, P. Wang, Y. Chen, X. Luo, Injectable self-healing hydrogels containing CuS nanoparticles with abilities of hemostasis, antibacterial activity, and promoting wound healing, ACS Biomater. Sci. Eng. 7 (1) (2020) 335–349.
[38] J. Qu, X. Zhao, P.X. Ma, B. Guo, pH-responsive self-healing injectable hydrogel based on N-carboxyethyl chitosan for hepatocellular carcinoma therapy, Acta Biomater. 58 (2017) 168–180.
[39] S. Thakur, O.A. Arotiba, Synthesis, swelling and adsorption studies of a pH-responsive sodium alginate–poly (acrylic acid) superabsorbent hydrogel, Polym. Bull. 75 (10) (2018) 4587–4606.
[40] Q. Li, Z. Feng, H. Song, J. Zhang, A. Dong, D. Kong, W. Wang, P. Huang, 19 F magnetic resonance imaging enabled real-time, non-invasive and precise localization and quantification of the degradation rate of hydrogel scaffolds in vivo, Biomater. Sci. 8 (12) (2020) 3301–3309.
[41] R. Xu, H. Xia, W. He, Z. Li, J. Zhao, B. Liu, Y. Wang, Q. Lei, Y. Kong, Y. Bai, Controlled water vapor transmission rate promotes wound-healing via wound re-epithelialization and contraction enhancement, Sci. Rep. 6 (1) (2016) 1–12.
[42] B. Yang, J. Song, Y. Jiang, M. Li, J. Wei, J. Qin, W. Peng, F.L.p. Lasaosa, Y. He, H. Mao, Injectable adhesive self-healing multicross-linked double-network hydrogel facilitates full-thickness skin wound healing, ACS Appl. Mater. Interfaces 12 (52) (2020) 57782–57797.
[43] N. Pan, J. Qin, P. Feng, Z. Li, B. Song, Color-changing smart fibrous materials for naked eye real-time monitoring of wound pH, J. Mater. Chem. B 7 (16) (2019) 2626–2633.
[44] S. Tavakoli, H. Mokhtari, M. Kharaziha, A. Kermanpur, A. Talebi, J. Moshtaghian, A multifunctional nanocomposite spray dressing of Kappa-carrageenan-polydopamine modified ZnO/L-glutamic acid for diabetic wounds, Mater. Sci. Eng. C 111 (2020), 110837.
[45] A. Rautela, J. Rani, Green synthesis of silver nanoparticles from Tectona grandis seeds extract: characterization and mechanism of antimicrobial action on different microorganisms, Journal of Analytical Science and Technology 10 (1) (2019) 1–10.

[46] M. Yan, J. Shi, S. Tang, G. Zhou, J. Zeng, Y. Zhang, H. Zhang, Y. Yu, J. Guo, Preparation of high-strength and high-toughness biomass medical films based on a polydopamine dynamically united calcium alginate/carboxymethyl chitosan dual network, New J. Chem. 45 (32) (2021) 14469–14482.
[47] W. Ding, J. Zhou, Y. Zeng, Y.-n. Wang, B. Shi, Preparation of oxidized sodium alginate with different molecular weights and its application for crosslinking collagen fiber, Carbohydr. Polym. 157 (2017) 1650–1656.
[48] M. Nara, H. Morii, M. Tanokura, Coordination to divalent cations by calcium-binding proteins studied by FTIR spectroscopy, Biochim. Biophys. Acta, Biomembr. 1828 (10) (2013) 2319–2327.
[49] M. Mizuguchia, M. Narab, K. Kawanoa, K. Nitta, FT-IR study of the Ca2+− binding to bovine oc-lactalbumin, FEBS Lett. 417 (1997) 153–156.
[50] H. Chen, X. Xing, H. Tan, Y. Jia, T. Zhou, Y. Chen, Z. Ling, X. Hu, Covalently antibacterial alginate-chitosan hydrogel dressing integrated gelatin microspheres containing tetracycline hydrochloride for wound healing, Mater. Sci. Eng. C 70 (2017) 287–295.
[51] S. Bykkam, M. Ahmadipour, S. Narisngam, V.R. Kalagadda, S.C. Chidurala, Extensive studies on X-ray diffraction of green synthesized silver nanoparticles, Adv. Nanoparticles 4 (1) (2015) 1–10.
[52] M. Zhang, X. Qiao, W. Han, T. Jiang, F. Liu, X. Zhao, Alginate-chitosan oligosaccharide-ZnO composite hydrogel for accelerating wound healing, Carbohydrate Polym. 266 (2021), 118100.
[53] Y. Chen, R. Zhang, B. Zheng, C. Cai, Z. Chen, H. Li, H. Liu, A biocompatible, stimuli-responsive, and injectable hydrogel with triple dynamic bonds, Molecules 25 (13) (2020) 3050.
[54] L. Ma, W. Su, Y. Ran, X. Ma, Z. Yi, G. Chen, X. Chen, Z. Deng, Q. Tong, X. Wang, Synthesis and characterization of injectable self-healing hydrogels based on oxidized alginate-hybrid-hydroxyapatite nanoparticles and carboxymethyl chitosan, Int. J. Biol. Macromol. 165 (2020) 1164–1174.
[55] M.C. García, A.A. Aldana, L.I. Tártara, F. Alovero, M.C. Strumia, R.H. Manzo, M. Martinelli, A.F. Jimenez-Kairuz, Bioadhesive and biocompatible films as wound dressing materials based on a novel dendronized chitosan loaded with ciprofloxacin, Carbohydr. Polym. 175 (2017) 75–86.
[56] E. Jain, L. Hill, E. Canning, S.A. Sell, S.P. Zustiak, Control of gelation, degradation and physical properties of polyethylene glycol hydrogels through the chemical and physical identity of the crosslinker, J. Mater. Chem. B 5 (14) (2017) 2679–2691.
[57] H. Pan, D. Fan, Z. Duan, C. Zhu, R. Fu, X. Li, Non-stick hemostasis hydrogels as dressings with bacterial barrier activity for cutaneous wound healing, Mater. Sci. Eng. C 105 (2019), 110118.
[58] K. Nuutila, Elof Eriksson, Moist wound healing with commonly available dressings, Adv. Wound Care 10 (12) (2021) 685–698. Moist wound healing with commonly available dressings, Advances in Wound Care 10(12) (2021) 685-698.
[59] J. Lei, L. Sun, P. Li, C. Zhu, Z. Lin, V. Mackey, D.H. Coy, Q. He, The wound dressings and their applications in wound healing and management, 4, Health Sci. J. 13 (4) (2019) 1–8.
[60] L.A. Schneider, A. Korber, S. Grabbe, J. Dissemond, Influence of pH on wound-healing: a new perspective for wound-therapy? Arch. Dermatol. Res. 298 (9) (2007) 413–420.
[61] R. Priyadarshi, P. Ezati, J.-W. Rhim, Recent advances in intelligent food packaging applications using natural food colorants, ACS Food Science & Technology 1 (2) (2021) 124–138.
[62] C. Wu, Y. Li, J. Sun, Y. Lu, C. Tong, L. Wang, Z. Yan, J. Pang, Novel konjac glucomannan films with oxidized chitin nanocrystals immobilized red cabbage anthocyanins for intelligent food packaging, Food Hydrocolloids 98 (2020), 105245.
[63] N. Ghareaghajlou, S. Hallaj-Nezhadi, Z. Ghasempour, Red cabbage anthocyanins: stability, extraction, biological activities and applications in food systems, Food Chem. 365 (2021), 130482.
[64] B. Mirani, E. Pagan, B. Currie, M.A. Siddiqui, R. Hosseinzadeh, P. Mostafalu, Y.S. Zhang, A. Ghahary, M. Akbari, An advanced multifunctional hydrogel-based dressing for wound monitoring and drug delivery, Advanced healthcare materials 6 (19) (2017), 1700718.
[65] Y.-K. Lee, S.-Y. Lee, A colorimetric alginate-catechol hydrogel suitable as a spreadable pH indicator, Dyes Pigments 108 (2014) 1–6.
[66] A.A. Arafa, A.A. Nada, A.Y. Ibrahim, M.K. Zahran, O.A. Hakeim, Greener therapeutic pH-sensing wound dressing based on Curcuma Longa and cellulose hydrogel, Eur. Polym. J. 159 (2021), 110744.
[67] J. Wang, J. Wei, S. Su, J. Qiu, Z. Hu, M. Hasan, E. Vargas, M. Pantoya, S. Wang, Thermal-recoverable tough hydrogels enhanced by porphyrin decorated graphene oxide, Nanomaterials 9 (10) (2019) 1487.
[68] J. Qu, X. Zhao, Y. Liang, T. Zhang, P.X. Ma, B. Guo, Antibacterial adhesive injectable hydrogels with rapid self-healing, extensibility and compressibility as wound dressing for joints skin wound healing, Biomaterials 183 (2018) 185–199.
[69] A. Kalra, A. Lowe, A. Al-Jumaily, Mechanical behaviour of skin: a review, J. Mater. Sci. Eng. 5 (4) (2016), 1000254.
[70] Y. Yue, X. Wang, Q. Wu, J. Han, J. Jiang, Assembly of polyacrylamide-sodium alginate-based organic-inorganic hydrogel with mechanical and adsorption properties, Polymers 11 (8) (2019) 1239.
[71] Y. Wang, Y. Xue, J. Wang, Y. Zhu, Y. Zhu, X. Zhang, J. Liao, X. Li, X. Wu, Y.-X. Qin, A composite hydrogel with high mechanical strength, fluorescence, and degradable behavior for bone tissue engineering, Polymers 11 (7) (2019) 1112.
[72] J. Wei, Jilong Wang, siheng su, shiren Wang, and jingjing qiu, tough and fully recoverable hydrogels, J. Mater. Chem. B 3 (26) (2015) 5284–5290.
[73] Y. Zhang, X. Zhao, W. Yang, W. Jiang, F. Chen, Q. Fu, Enhancement of mechanical property and absorption capability of hydrophobically associated polyacrylamide hydrogels by adding cellulose nanofiber, Mater. Res. Express 7 (1) (2020), 015319.
[74] N. Sreenivasachary, J.-M. Lehn, Gelation-driven component selection in the generation of constitutional dynamic hydrogels based on guanine-quartet formation, Proc. Natl. Acad. Sci. USA 102 (17) (2005) 5938–5943.
[75] H. Mokhtari, M. Kharaziha, F. Karimzadeh, S. Tavakoli, An injectable mechanically robust hydrogel of Kappa-carrageenan-dopamine functionalized graphene oxide for promoting cell growth, Carbohydr. Polym. 214 (2019) 234–249.
[76] Y. Tu, N. Chen, C. Li, H. Liu, R. Zhu, S. Chen, Q. Xiao, J. Liu, S. Ramakrishna, L. He, Advances in injectable self-healing biomedical hydrogels, Acta Biomater. 90 (2019) 1–20.
[77] F. Cuomo, M. Cofelice, F. Lopez, Rheological characterization of hydrogels from alginate-based nanodispersion, Polymers 11 (2) (2019) 259.
[78] J. Luo, X. Shi, L. Li, Z. Tan, F. Feng, J. Li, M. Pang, X. Wang, L. He, An injectable and self-healing hydrogel with controlled release of curcumin to repair spinal cord injury, Bioact. Mater. 6 (12) (2021) 4816–4829.
[79] M. Mehdizadeh, H. Weng, D. Gyawali, L. Tang, J. Yang, Injectable citrate-based mussel-inspired tissue bioadhesives with high wet strength for sutureless wound closure, Biomaterials 33 (32) (2012) 7972–7983.
[80] J. Deng, Y. Tang, Q. Zhang, C. Wang, M. Liao, P. Ji, J. Song, G. Luo, L. Chen, X. Ran, A bioinspired medical adhesive derived from skin secretion of Andrias davidianus for wound healing, Adv. Funct. Mater. 29 (31) (2019), 1809110.
[81] T.T.H. Thi, Y. Lee, S.B. Ryu, H.-J. Sung, K.D. Park, Oxidized cyclodextrin-functionalized injectable gelatin hydrogels as a new platform for tissue-adhesive hydrophobic drug delivery, RSC Adv. 7 (54) (2017) 34053–34062.
[82] J. Pang, S. Bi, T. Kong, X. Luo, Z. Zhou, K. Qiu, L. Huang, X. Chen, M. Kong, Mechanically and functionally strengthened tissue adhesive of chitin whisker complexed chitosan/dextran derivatives based hydrogel, Carbohydr. Polym. 237 (2020), 116138.
[83] Z. Bai, W. Dan, G. Yu, Y. Wang, Y. Chen, Y. Huang, C. Yang, N. Dan, Tough and tissue-adhesive polyacrylamide/collagen hydrogel with dopamine-grafted oxidized sodium alginate as crosslinker for cutaneous wound healing, RSC Adv. 8 (73) (2018) 42123–42132.
[84] M. Pandian, V. Selvaprithviraj, A. Pradeep, J. Rangasamy, In-situ silver nanoparticles incorporated N, O-carboxymethyl chitosan based adhesive, self-healing, conductive, antibacterial and anti-biofilm hydrogel, Int. J. Biol. Macromol. 188 (2021) 501–511.
[85] T. Chen, Y. Chen, H.U. Rehman, Z. Chen, Z. Yang, M. Wang, H. Li, H. Liu, Ultratough, self-healing, and tissue-adhesive hydrogel for wound dressing, ACS Appl. Mater. Interfaces 10 (39) (2018) 33523–33531.
[86] Z. Li, B. Li, X. Li, Z. Lin, L. Chen, H. Chen, Y. Jin, T. Zhang, H. Xia, Y. Lu, Ultrafast in-situ forming halloysite nanotube-doped chitosan/oxidized dextran hydrogels for hemostasis and wound repair, Carbohydr. Polym. 267 (2021), 118155.
[87] L. Gao, Y. Zhou, J. Peng, C. Xu, Q. Xu, M. Xing, J. Chang, A novel dual-adhesive and bioactive hydrogel activated by bioglass for wound healing, NPG Asia Mater. 11 (1) (2019) 1–11.
[88] K. Kim, J.H. Ryu, M.-Y. Koh, S.P. Yun, S. Kim, J.P. Park, C.-W. Jung, M.S. Lee, H.-I. Seo, J.H. Kim, Coagulopathy-independent, bioinspired hemostatic materials: a full research story from preclinical models to a human clinical trial, Sci. Adv. 7 (13) (2021), eabc9992.
[89] L. Gao, J. Chen, W. Feng, Q. Song, J. Huo, L. Yu, N. Liu, T. Wang, P. Li, W. Huang, A multifunctional shape-adaptive and biodegradable hydrogel with hemorrhage control and broad-spectrum antimicrobial activity for wound healing, Biomater. Sci. 8 (24) (2020) 6930–6945.
[90] H. Cheng, C. Li, Y. Jiang, B. Wang, F. Wang, Z. Mao, H. Xu, L. Wang, X. Sui, Facile preparation of polysaccharide-based sponges and their potential application in wound dressing, J. Mater. Chem. B 6 (4) (2018) 634–640.
[91] M. Suneetha, K.M. Rao, S.S. Han, Mussel-inspired cell/tissue-adhesive, hemostatic hydrogels for tissue engineering applications, ACS Omega 4 (7) (2019) 12647–12656.
[92] H. Geng, Q. Dai, H. Sun, L. Zhuang, A. Song, F. Caruso, J. Hao, J. Cui, Injectable and sprayable polyphenol-based hydrogels for controlling hemostasis, ACS Appl. Bio Mater. 3 (2) (2020) 1258–1266.
[93] E. Lamei, M. Hasanzadeh, Fabrication of chitosan nanofibrous scaffolds based on tannic acid and metal-organic frameworks for hemostatic wound dressing applications, Int. J. Biol. Macromol. 208 (2022) 409–420.
[94] M. Grkovic, D.B. Stojanovic, V.B. Pavlovic, M. Rajilic-Stojanovic, M. Bjelovic, P.S. Uskokovic, Improvement of mechanical properties and antibacterial activity of crosslinked electrospun chitosan/poly (ethylene oxide) nanofibers, Compos. B Eng. 121 (2017) 58–67.
[95] X. Zhang, Y. Pan, S. Li, L. Xing, S. Du, G. Yuan, J. Li, T. Zhou, D. Xiong, H. Tan, Doubly crosslinked biodegradable hydrogels based on gellan gum and chitosan for drug delivery and wound dressing, Int. J. Biol. Macromol. 164 (2020) 2204–2214.
[96] T.J. Silhavy, D. Kahne, S. Walker, The bacterial cell envelope, Cold Spring Harbor Perspect. Biol. 2 (5) (2010) a000414.
[97] X. He, X. Liu, J. Yang, H. Du, N. Chai, Z. Sha, M. Geng, X. Zhou, C. He, Tannic acid-reinforced methacrylated chitosan/methacrylated silk fibroin hydrogels with multifunctionality for accelerating wound healing, Carbohydr. Polym. 247 (2020), 116689.
[98] M. Lopez-Carrizales, E. Mendoza-Mendoza, R.D. Peralta-Rodriguez, M.A. Pérez-Díaz, D. Portales-Pérez, M. Magaña-Aquino, A. Aragón-Piña, R. Infante-Martínez, E.D. Barriga-Castro, R. Sánchez-Sánchez, G.A. Martinez-Castañon, Characterization, antibiofilm and biocompatibility properties of chitosan hydrogels loaded with silver nanoparticles and ampicillin: an alternative

protection to central venous catheters, Colloids Surf. B Biointerfaces 196 (2020), 111292.
[99] M. Khamrai, S.L. Banerjee, S. Paul, A.K. Ghosh, P. Sarkar, P.P. Kundu, A mussel mimetic, bioadhesive, antimicrobial patch based on dopamine-modified bacterial cellulose/rGO/Ag NPs: a green approach toward wound-healing applications, ACS Sustain. Chem. Eng. 7 (14) (2019) 12083–12097.
[100] K. Kawata, M. Osawa, S. Okabe, In vitro toxicity of silver nanoparticles at noncytotoxic doses to HepG2 human hepatoma cells, Environ. Sci. Technol. 43 (15) (2009) 6046–6051.
[101] Y.K. Jo, J.H. Seo, B.H. Choi, B.J. Kim, H.H. Shin, B.H. Hwang, H.J. Cha, Surface-independent antibacterial coating using silver nanoparticle-generating engineered mussel glue, ACS Appl. Mater. Interfaces 6 (22) (2014) 20242–20253.
[102] A. Hernández-Rangel, P. Silva-Bermudez, B.L. Espana-Sanchez, E. Luna-Hernández, A. Almaguer-Flores, C. Ibarra, V.I. Garcia-Perez, C. Velasquillo, G. Luna-Barcenas, Fabrication and in vitro behavior of dual-function chitosan/silver nanocomposites for potential wound dressing applications, Mater. Sci. Eng. C 94 (2019) 750–765.
[103] N. Hashim, M. Paramasivam, J.S. Tan, D. Kernain, M.H. Hussin, N. Brosse, F. Gambier, P.B. Raja, Green mode synthesis of silver nanoparticles using Vitis vinifera's tannin and screening its antimicrobial activity/apoptotic potential versus cancer cells, Mater. Today Commun. 25 (2020), 101511.
[104] P.V. AshaRani, G. Low Kah Mun, M.P. Hande, S. Valiyaveettil, Cytotoxicity and genotoxicity of silver nanoparticles in human cells, ACS Nano 3 (3) (2009) 279–290.
[105] X. Feng, X. Hou, C. Cui, S. Sun, S. Sadik, S. Wu, F. Zhou, Mechanical and antibacterial properties of tannic acid-encapsulated carboxymethyl chitosan/polyvinyl alcohol hydrogels, Engineered Regeneration 2 (2021) 57–62.
[106] Z. Bai, T. Wang, X. Zheng, Y. Huang, Y. Chen, W. Dan, High strength and bioactivity polyvinyl alcohol/collagen composite hydrogel with tannic acid as cross-linker, Polym. Eng. Sci. 61 (1) (2021) 278–287.
[107] S. Singh, O.F. Nwabor, D.M. Syukri, S.P. Voravuthikunchai, Chitosan-poly (vinyl alcohol) intelligent films fortified with anthocyanins isolated from Clitoria ternatea and Carissa carandas for monitoring beverage freshness, Int. J. Biol. Macromol. 182 (2021) 1015–1025.